

# Dynamic simulation of freely-draining, flexible bead-rod chains: Start-up of extensional and shear flow<sup>1</sup>

Patrick S. Doyle, Eric S.G. Shaqfeh \*

*Department of Chemical Engineering, Stanford University, Stanford, CA 94305-5025, USA*

Received 14 June 1997

---

## Abstract

We present a study of the rheology and optical properties during the start-up of uniaxial extensional and shear flow for freely-draining, Kramers bead-rod chains using Brownian dynamics simulations. The viscous and elastic contributions to the polymer stress are unambiguously determined via methods developed in our previous publication [1]. The elastic contribution to the polymer stress is much larger than the viscous contribution beyond a time of  $5.3\lambda_1/N^2$  where  $N$  is the number of beads in the chain and  $\lambda_1$  is the longest relaxation time of the chain. For small  $Wi$  (at arbitrary strains) and for small strains (at arbitrary  $Wi$ ) the stress-optic law is found to be valid. The stress-optic coefficients based on the shear stress and first normal stress difference are equal for all  $Wi$  (even when the stress-optic law is not valid) suggesting the stress-optic coefficient is in general a scalar quantity rather than its most general form as a fourth order tensor.

We show that a multimode FENE-PM or Rouse model describes the rheology of the bead-rod chains at small strains, while the FENE dumbbell is an accurate model at larger strains. We compare the FENE-PM and FENE model to experimental extensional stress data of dilute polystyrene solutions and find that a multimode FENE-PM with a Zimm relaxation spectrum describes the data well at small strains while a FENE dumbbell with a conformation dependent drag is in quantitative agreement at larger strains. © 1998 Elsevier Science B.V. All rights reserved.

*Keywords:* Bead-rod chains; Extensional flow; Shear flow

---

## 1. Introduction

The study and development of numerical techniques to solve non-Newtonian fluid mechanics problems has undergone dramatic changes in recent years with the introduction of the CONNFFESSIT [2–4] and Brownian configurational fields [4,5] methods which do not necessitate closure approximations for nonlinear dumbbell models, such as the FENE model. However,

---

\* Corresponding author. Fax: +1 415 7239780.

<sup>1</sup> Dedicated to the memory of Professor Gianni Astarita

even these methods still involve relatively simple bead-spring models as well as a limited number of modes or springs. The understanding of the ‘physics in the spring’ requires further study of the dilute solution rheology of polymers and is of great interest and concern in the literature [6–9]. For weak flows in which the polymer configuration is only slightly perturbed from the equilibrium configuration, linear dumbbell models show good agreement with experiments [10,11]. Experimental data for Lagrangian unsteady flows with a substantial extensional component have been successfully described via calculations using the nonlinear FENE model but using physically unrealistic FENE parameters [12–15]. The failure of dumbbell models in strong flows has been attributed to an extra viscous polymer stress [7,8] which is absent in most polymer models.

There have been several studies which have suggested models and scalings for viscous polymer stresses in the presence of unsteady strong flows. Kuhn and Kuhn [16] developed the internal viscosity model (IV model) which accounts for the molecular rigidity of a polymer and frictional barriers to rapid, short length scale distortions. The internal viscosity dumbbell model has a force acting on the beads which is proportional to the rate of deformation of the spring connecting the two beads [10,11]. Though the internal viscosity force is based on molecular concepts, the strength cannot be readily estimated from the molecular structure of the polymer [11]. In the limit of an infinite internal viscosity and several bead-springs, the model is similar to the bead-rod model. Manke and Williams [17] found good agreement between the complex viscosity of a modified multibead-IV model and bead-rod chains. However, in extensional flow the multibead-IV model fails to predict chain unravelling or extension [18] which is observed in the bead-rod model [8,19]. In transient shear flow, the multibead-IV model predicts large oscillations in the approach to the steady state shear viscosity and first normal stress coefficient [20] which have not been observed experimentally [10]. Additionally, the partitioning of the polymer stress into elastic and viscous components [1,21] has not been examined for the multibead-IV model.

Most other models of viscous stresses for flexible polymers have used rigidly constrained beads which result in viscous stresses (in addition to the usual Brownian stresses) analogous to that in a rigid rod suspension [21]. Acierno et al. [19] were among the first to use a non-Brownian bead-rod model to develop a physical basis for viscous polymer stresses in extensional flow. King and James [22] later suggested a frozen-necklace model in which a Rouse chain in extensional flow becomes frozen into a fixed configuration. In both the bead-rod and frozen-necklace models the viscous polymer stress is due to the rigid constraints imposed on the polymer motion. Rallison and Hinch [7] showed the large viscous stresses for non-Brownian bead-rod chains in extensional flow are due to backloops which form during the unravelling of the chain. Guided by the backloop concept, Larson [23] developed a novel kink dynamics model in which a polymer unravels like a one dimensional non-Brownian string and viscous forces arise due to the inextensibility of the string. Hinch [8] performed both Brownian and non-Brownian simulations of bead-rod chains along with the kink-dynamics model and concluded that the polymer stress in strong flows is mostly viscous. The viscous polymer stress was found to scale with  $R_g^4/N$  where  $R_g$  is the chain radius of gyration and  $N$  is the number of beads. His simulation method for the Brownian chains was not rigorous and was later modified [24] to study the relaxation of bead-rod chains from an initially unraveled configuration. Thus these previous bead-rod studies fail to unambiguously determine the relative magnitudes of the viscous and the elastic polymer stresses.

Previously we developed a means to separate the elastic and viscous contribution to the polymer stress for Kramers' bead-rod chains [1]. In steady shear and extensional flow we determined that the stress is dominated by the elastic component for all reasonable  $Wi$  where the  $Wi$  is the product of the shear (or extension) rate and the longest relaxation time of the chain. In extensional flow, the viscous stress becomes as large as the elastic at  $Wi = 0.06N^2$  [1]. Recently, Rallison [9] has numerically confirmed the steady-state stress partitioning for small chains ( $N \leq 10$ ) in planar extensional flow but in his calculations for the start-up of elongational flow he used a bead-stiff-spring model and thus was unable to compute a viscous polymer stress. For Rallison's start-up simulations he concluded that a significant viscous polymer stress exists in transient flows which scales with  $R_g^2$ . This conclusion is based on how the polymer stress scales with the radius of gyration tensor and not by determining the actual partitioning of the polymer stresses. He does suggest the stress that he terms as 'viscous' may actually be an elastic stress with a fast relaxation time. In the present study, we use our simulation method [1] and unambiguously determine the partitioning of the stresses in transient flows for bead-rod chains.

The bead-rod chain is a coarse grain model of an atomistic polymer chain but is still too cumbersome for the numerical solution of most non-Newtonian fluid mechanics problems. Instead simple bead-spring models are most often employed. The original development of the spring force in these models is based on the entropic restoring force for a bead-rod chain [25]. The force required to increase the chain end-to-end separation is linear in the end-to-end separation for small deformations [25] and is given by the inverse Langevin function for large distortions [26]. The Hookean spring force corresponds to the linear limit and the FENE spring force is a numerical approximation of the nonlinear limit [27]. There is thus a direct relationship between the spring constants and the bead-rod chain parameters. These models can be modified to include multiple beads connected consecutively by springs (Rouse and multibead FENE models). The polymer stress in the FENE and Rouse model is purely elastic because the spring force law is derived from entropic restoring forces. The Rouse model fails in strong flows due to an unbound growth of the chain microstructure [10,11]. Comparisons of the FENE model to experimental data have usually made use of the Peterlin approximation [28] to preaverage the nonlinear FENE force, commonly referred to as the FENE-P model. Small values for the maximum extensibility of the dumbbell were needed to obtain quantitative agreement with experiments [12–15]. While it is clear that the finite extensibility of the FENE dumbbell is physically sensible, the magnitude of the nonlinear elastic stresses in strong flows and the proper manner to choose the maximum extensibility of the dumbbell is not clear. A different test of the FENE model is a comparison to the more complicated bead-rod model from which it was originally derived. Previously [1], we demonstrated that FENE dumbbells are in good agreement with the steady-state shear and elongational rheology of bead-rod chains, but we did not compute transient properties of either model.

Experimentally one can measure polymer stresses using birefringence if the stress-optic law is valid [29]. Experiments have confirmed the validity of the stress-optic law for weak shear flow [30], while under strong flow conditions the stress-optic law is not generally valid [31–33]. Smyth et al. [34] have confirmed the existence of viscous stresses for semidilute solutions of semirigid polymers in steady shear flow and have shown that the stress-optic law is valid for the elastic part of the polymer stress. An intriguing set of filament stretching experiments using Boger fluids have recently been performed by Spiegelberg and McKinley [33] in which the stress-optic law

during the inception of extensional flow was valid up to a certain strain. It is not currently known whether the failure of the stress-optic law for flexible polymer solutions in strong flows is due to an additional polymer viscous stress or a nonlinear elastic polymer stress. Determining this will not only aid in the fundamental understanding of polymer stresses in strong flows but is the first step in developing a modified stress-optic relationship for highly extended dilute polymers.

In this paper we present results for the transient stresses and birefringence of dilute bead-rod chains in shear and uniaxial elongational flow. We concentrate on three main points: partitioning of the stresses into viscous and elastic components, comparison to the FENE dumbbell, Rouse chains and FENE-PM model and the validity of the stress-optic law. Start-up of uniaxial extensional and shear flow is presented for a wide range of  $Wi$  and  $N$ . The polymer stress is separated into its viscous and elastic components and we determine the time scale and Flow strength over which the viscous contribution is significant. We determine when and why the stress-optic law begins to fail. The simulation results for the bead-rod chains are compared to Brownian dynamics simulations of FENE dumbbells, numerical calculations of a multimode Rouse chain and a multimode FENE-PM chain. A critical assessment is made of the bead-spring models and whether their deficiencies are created by preaveraging approximations, coarse graining, or more fundamental physical problems. The extensional viscosity predicted by the FENE and FENE-PM models is compared to experimental data of dilute polystyrene solutions.

## 2. Bead-rod polymer model

In this study the polymer is modeled as a bead-rod chain, where the beads act as sources of friction and the rods serve as constraints to hold successive beads at a constant relative distance. Physically the rod length scale corresponds to a Kuhn step in a polymer molecule and is a measure of the chain rigidity. We have chosen to examine the bead-rod model for two reasons. First, the bead-rod model is the fundamental starting point for most constitutive equations and simple dumbbell models [10,11,21]. Second, the rigid nature of the rods gives rise to viscous stresses in addition to elastic stresses [21]. Thus, we can unambiguously determine the partitioning of the stresses into its viscous and elastic components.

The simulation technique has been discussed extensively in our previous paper [1] and a brief overview is provided below. We employ index notation throughout our discussion and Greek superscripts will refer to bead numbers. A stochastic differential equation used to compute chain trajectories can be derived by considering the relevant forces on the chain: hydrodynamic ( $F_i^{h,v}$ ), Brownian ( $F_i^{br,v}$ ) and constraint ( $F_i^{c,v}$ ). Neglecting inertia, the forces on a bead are summed and set at zero.

The hydrodynamic force on a bead is assumed to be linear in the slip velocity between the bead and the solvent velocity at the bead center. Thus,

$$F_i^{h,v} = -\zeta(\dot{r}_i^v - u_i^\infty(r_i^v)), \quad (1)$$

where  $\zeta$  is the drag on a bead,  $r_i^v$  is location of the center of bead  $v$ ,  $\dot{r}_i^v$  is the velocity of bead  $v$  and  $u_i^\infty(r_i^v)$  is the undisturbed solvent velocity. We have neglected any disturbance velocity created by the beads. In our studies we limited ourselves to linear flows where the shear rate,  $\dot{\gamma}$ , or extension rate,  $\dot{\epsilon}$ , rate is defined by:

$$\frac{\partial u_i^\infty}{\partial x_j} = \begin{cases} \kappa_{ij} \dot{\gamma} & \text{shear flow,} \\ \kappa_{ij} \dot{\epsilon} & \text{uniaxial extensional flow,} \end{cases} \quad (2)$$

and  $\kappa_{ij}$  is defined by

$$\kappa_{ij} = \begin{cases} \delta_{i1} \delta_{j2} & \text{shear flow,} \\ \delta_{i1} \delta_{j1} - 0.5 \delta_{i2} \delta_{j2} - 0.5 \delta_{i3} \delta_{j3} & \text{uniaxial extensional flow.} \end{cases} \quad (3)$$

We assume that during each time step a bead experiences numerous collisions with the solvent molecules. Neglecting the effects due to the constraints, these Brownian forces are approximated as a  $\delta$  correlated, white noise process [35]. A discrete form for the Brownian forces during an individual time step beginning at time  $t$  and ending at time  $t + \delta t$  is

$$\langle F_i^{br,v}(\tau) \rangle = 0 \quad (4)$$

$$\langle F_i^{br,v}(\tau) F_j^{br,\mu}(\tau) \rangle = \frac{2kT\xi \delta_{v\mu} \delta_{ij}}{\delta t} \quad (5)$$

where  $\tau$  is equal to  $t + 1/2\delta t$  which corresponds to a Stratonovich interpretation of the stochastic term [35]. The  $2kT\xi$  term results from satisfying the fluctuation dissipation theorem in the absence of constraints [36]. We note that when the Brownian forces are included in this manner they have a magnitude proportional to  $1/\sqrt{\delta t}$  and the sample trajectories will be continuous but the time derivative of the paths (or the velocity) will be discontinuous.

The constraint forces are calculated using the method of Lagrangian multipliers employed by Ryckaert [37] and Liu [38]. The constant force on bead  $v$  is

$$F_i^{c,v} = T^v u_i^v - T^{v-1} u_i^{v-1} \quad (6)$$

where  $T^v$  are the  $N - 1$  undetermined Lagrangian multipliers,  $u_i^v = (\tau_i^{v+1} - \tau_i^v)/a$  and  $a$  is the length of the connecting rod. Physically  $T^v$  corresponds to tensions in the connecting rods arising from both the deterministic (flow) and stochastic (Brownian) forces. The Lagrangian constraints are chosen to satisfy the constraint of constant rod length at the end of a time step.

An iterative scheme is used to calculate the trajectories of the chains in our simulations. We have previously shown that this scheme is equivalent to a midpoint algorithm [1]. At the beginning of each time step an unconstrained move, denoted by  $t^*$ , is taken:

$$r_i^v(t^*) = r_i^v(t) + \left[ u_i^\infty(r_i^v(t)) + \frac{F_i^{br,v}}{\xi} \right] \delta t. \quad (7)$$

The bead positions are subject to the constraint

$$[r_i^{v+1}(t + \delta t) - r_i^v(t + \delta t)][r_i^{v+1}(t + \delta t) - r_i^v(t + \delta t)] - a^2 < \varphi \quad (8)$$

where  $\varphi \ll a^2$  and  $r_i^v(t + \delta t)$  is given by

$$r_i^v(t + \delta t) = r_i^v(t^*) + \left[ \frac{T^v u_i^v - T^{v-1} u_i^{v-1}}{\xi} \right] \delta t. \quad (9)$$

Combining Eqs. (7)–(9) leads to  $N - 1$  nonlinear equations for the tensions. The nonlinear term is small relative to the linear terms and the  $N - 1$  linear equations can be solved iteratively [1,38]. The equations (1–9) form the basis for computing trajectories of a chain in a given flow field and are referred to as the trajectory evolution equations.

To begin a simulation a random walk polymer configuration is generated by choosing successive bead positions from random vectors distributed over the surface of a sphere. Since the equilibrium configuration of a bead-rod chain is not a random walk [10,39,40], we allow the chain to equilibrate for  $10^5 \times 10^6$  time steps during which the solvent velocity is set to zero. The solvent velocity is then set to the desired value at  $t=0$ . Ensemble averages are taken over populations of 100–4000 chains. For the range of  $Wi$  we simulated, the time step was set equal to or less than  $0.001\zeta a^2/kT$ . Additionally, in the extensional flow simulations we decreased the size of the time step during a simulation as the strain and tensions in the connecting rods increased.

### 2.1. Polymer stress calculation

Care must be taken in calculating the polymer stress in a system with rigid constraints. Furthermore, the algorithm for stress calculation must be consistent with the simulation algorithm in handling the stochastic forces. Algorithms which necessitate time derivatives of spatial coordinates of beads, such as the Giesekus stress tensor [10], cannot be used due to the discontinuous velocity of the beads. We employ a novel noise filtering technique [1] which eliminates  $O(1/\sqrt{\delta t})$  noise in the stress evaluation and is consistent with the Stratonovich interpretation of the Brownian forces employed in the trajectory evolution algorithm. Specific details of the technique can be found elsewhere [1].

The total stress in a flowing suspension of model polymers is the sum of the polymer and solvent contributions,

$$\sigma_{ij} = \sigma_{ij}^p + \sigma_{ij}^s \quad (10)$$

and can be expressed as [10]

$$\sigma_{ij} = \tau_{ij} - P\delta_{ij} = \tau_{ij}^p - P^p\delta_{ij} + \tau_{ij}^s - P^s\delta_{ij} \quad (11)$$

where  $\tau_{ij} = \tau_{ij}^p + \tau_{ij}^s$  and  $P = P^p + P^s$ .  $\tau_{ij}$  is defined to be zero equilibrium and  $P$  is an isotropic pressure contribution. The polymer contribution to the stress is given by the Kramers–Kirkwood stress tensor as the moment of the hydrodynamic forces [10]. Due to the force balance on the chain, this can be expressed in terms of the Brownian and constraint forces

$$\tau_{ij}^p = -n_p \sum_{v=1}^N \langle R_i^v F_j^{br,v} + R_i^v F_j^{c,v} \rangle \quad (12)$$

where  $n_p$  is the number density of polymer chains and  $R_i^v$  is the position of bead  $v$  relative to the chain center of mass. Employing our noise filtering scheme, the polymer stress is calculated as

$$\begin{aligned} & -n_p \left\langle \left[ \frac{R_i^v(t+\delta t) + R_i^v(t)}{2} \right] [F_j^{c,v}(t) - F_j^{*,v}(t)] + \left[ \frac{R_i^v(t+\delta t) - R_i^v(t)}{2} \right] F_j^{*,v}(t) \right. \\ & \left. + \left[ \frac{R_i^v(t+\delta t) - R_i^v(t)}{2} \right] F_j^{b,v}(t + \delta t/2) \right\rangle. \end{aligned} \quad (13)$$

$F_i^{*,v}$  denotes the constraint forces derived including only Brownian forces in the trajectory evolution equations and determining the Lagrangian multipliers subject to the constraint that the link velocity is perpendicular to the link orientation at the beginning of a time step. Without

the filtering technique, we would typically have to use ensembles which are at least 10–20 times larger to obtain similar results. The viscous component of the polymer stress is much easier to calculate since it does not directly involve stochastic forces. It is important to remember that the stochastic forces contribute indirectly since they help to determine the chain configuration. For a given chain configuration and flow field, the viscous stress is obtained by setting the Brownian forces to zero and calculating the constraint forces. Since the flow field is not stochastic, we impose the constraint that the link velocity is perpendicular to the link direction at the beginning of a time step and noise filtering is not necessary. Denoting these constraint forces as  $F_i^{c,visc,v}$ , the viscous stress is

$$\tau_{ij}^{p,visc} = -n_p \sum_{v=1}^N \langle R_i^v F_j^{c,visc,v} \rangle. \quad (14)$$

The elastic or Brownian stress is then the difference in the total and the viscous stress.

## 2.2. Optical anisotropy and stress-optic law

The birefringence is a measure of the anisotropy in the index of refraction of a medium [29]. For polymer solutions, the birefringence measures the degree of orientation of the polymer on the length scale of a Kuhn step [11,29]. Each rod in the chain is assumed to act as an individual polarizing element with polarizability  $\alpha_1$  parallel to the rod and  $\alpha_2$  perpendicular. The dimensionless polymer contribution to the index of refraction tensor  $n_{ij}^p$  is [11]

$$n_{ij}^p = \sum_{v=1}^{N-1} u_i^v u_j^v, \quad (15)$$

where  $u_i^v$  is the orientation of rod  $v$ ,  $u_i^v = R_i^{v+1} - R_i^v$ .  $n_{ij}^p$  has been made dimensionless with  $n_p A (\alpha_1 - \alpha_2)$ .  $A = (4\pi/3)((n^2 + 2)^2/6n)$  and  $n$  is the isotropic part of the index of refraction [11].

The birefringence,  $\Delta'$ , is the difference in the principle eigenvalues of the index of refraction tensor. For light propagating along the '3' direction the birefringence is [29]

$$\Delta' = \sqrt{\left[ \sum_{v=1}^{N-1} \langle u_1^v u_1^v - u_2^v u_2^v \rangle \right]^2 + 4 \left[ \sum_{v=1}^{N-1} \langle u_1^v u_2^v \rangle \right]^2}, \quad (16)$$

where  $\Delta'$  has been made dimensionless with  $n_p A (\alpha_1 - \alpha_2)$ . The extinction angle,  $\chi$ , measures the orientation of the principal axis from the '1' direction [29]:

$$\tan(2\chi) = \frac{2 \sum_{v=1}^{N-1} \langle u_1^v u_2^v \rangle}{\sum_{v=1}^{N-1} \langle u_1^v u_1^v - u_2^v u_2^v \rangle} \quad (17)$$

For shear and uniaxial extensional flow, the dimensionless birefringence will be zero at equilibrium and have a maximum possible value of  $N - 1$ . The extinction angle in shear flow for small  $Wi$  is initially  $45^\circ$  and can decrease to a minimum of  $0^\circ$ . Due to the symmetry of extensional flow, the extinction angle is a constant for all  $Wi$  and is equal to zero when measured relative to the principal axis. Note that one cannot deduce the degree to which a chain has been extended from the birefringence unless you can prove by some other means how the

chains are extended since a fully aligned chain and a chain which is folded back on itself can have the same birefringence.

Experimentally, the birefringence can be a very useful non-invasive measure of the polymer stress if the stress-optic law is valid for the system [11,41,42]. We define a stress optic coefficient by the relation:

$$n_{ij}^p = C\sigma_{ij}^p. \quad (18)$$

If the stress-optic law is valid then  $C$  will be a constant. Kuhn and Grun [26] have shown that for small deformations of a bead-rod chain, the stress-optic law will hold and  $C$  will take on a value of 0.2. Previously [1], we confirmed this constant coefficient for steady linear flows at small  $Wi$ .

### 2.3. Dimensions

Unless otherwise noted all quantities will be presented in dimensionless terms. Lengths are scaled on the bead separation distance  $a$ , forces with  $kT/a$  and time with the single bead diffusion time scale  $\xi a^2/kT$ . The flow strength is characterized by the Weissenberg number,  $Wi = \lambda_1 \dot{\gamma}$  (or  $\lambda_1 \dot{\epsilon}$ ) where  $\lambda_1$  is the slowest relaxation time in the chain. In previous chain relaxation studies [1], we found that for large chains ( $N \geq 25$ )  $\lambda_1 = 0.0142N^2 \xi a^2/kT$ . The Weissenberg number is thus the ratio of the slowest relaxation process in the polymer chain to the flow time scale. We define another measure of the flow strength based on the single bead diffusion time as the Peclet number,  $Pe = \dot{\gamma} a^2/kT$ .

### 3. FENE dumbbell model

One of the simplest models for a polymer molecule is two beads joined by a spring. Kuhn and Grun [26] derived a spring force starting from a bead-rod chain by considering the force required to hold the two ends of a bead-rod chain with  $N$  beads at a fixed end-to-end vector  $Q_i$ . The force is proportional to an inverse Langevin function which diverges as the magnitude of  $Q_i$  approaches the chain contour length. A simpler empirical form was developed by Warner [27]:

$$F_i^{\text{FENE}} = \frac{HQ_i}{\left[1 - \left(\frac{Q_i}{Q_0}\right)^2\right]}, \quad (19)$$

which is referred to as the FENE spring force. The FENE spring force diverges as  $Q = \sqrt{Q_i Q_i}$  approaches the maximum extensibility of the dumbbell  $Q_0$ . The parameters  $H$  and  $Q_0$  are related to a bead-rod chain through the relations:

$$H = \frac{3kT}{(N-1)a^2}, \quad (20)$$

$$Q_0 = (N-1)a. \quad (21)$$

We have chosen to perform Brownian dynamics simulations of FENE dumbbells rather than use the closure approximation of the FENE-P model because it has recently been shown [43,44] that large differences exist between the models for transient flows. The relaxation time for the FENE dumbbell is  $\lambda_H = \zeta/4H$  where  $\zeta$  is the drag on one bead in the dumbbell and the dimensionless extensibility parameter is  $b = HQ_0^2/kT$ . For large  $N$ , the extensibility parameter  $b$  is equal to  $3N$ . We will refer to this value of  $b$  as the corresponding value for a bead-rod chain with  $N$  beads or alternatively, the expected value. In considering FENE dumbbells all lengths are made dimensionless with  $\sqrt{kT/H}$  and stress with  $n_p kT$ . A Weissenberg number for the dumbbell is defined by  $Wi^{\text{FENE}} = \lambda_H \dot{\gamma}$  (or  $\lambda_H \dot{\epsilon}$ ). We employ the semi-implicit predictor corrector method proposed by Öttinger [44,45] to solve for the trajectories of the dumbbells. Ensemble averages are taken over populations of  $10^4$  dumbbells. The dimensionless dumbbell stress is calculated using the Kramers stress tensor

$$\tau_{ij}^{\text{FENE}} = \langle Q_i F_j^{\text{FENE}} \rangle - \delta_{ij}. \quad (22)$$

The dimensionless birefringence for the FENE dumbbell is [11]

$$\Delta' = (1/5)[\langle Q_1 Q_1 - Q_2 Q_2 \rangle^2 + 4\langle Q_1 Q_2 \rangle^2]^{1/2}. \quad (23)$$

The FENE birefringence has been made dimensionless in the same manner as for the birefringence of the bead-rod chain, i.e. with  $n_p(\alpha_1 - \alpha_2)(4\pi/3)((n^2 + 2)^2/6n)$ . A maximum birefringence,  $\Delta' = b/5$ , occurs for a dumbbell aligned in the ‘1’ direction and stretched to maximum extension. Expressed in terms of  $N$ , the maximum birefringence is  $3/5N$  whereas for the bead-rod chain the maximum birefringence is  $N$ . The models differ at full extension because the FENE birefringence (or any elastic dumbbell) is derived on the assumption of a small distortion from a Gaussian coil [26]. Also, the dimensionless stress-optic coefficient for the FENE model is  $1/5$ .

#### 4. Rouse chain

The Rouse chain consists of a series of  $M + 1$  beads connected by  $M$  Hookean springs [10,46]. The spring force is the small deformation limit of the FENE spring force law and thus is only physically valid for small deformations of the chain. The model can be transformed into normal coordinates [46] and the constitutive equation consists of a series of uncoupled differential equations [10]

$$\tau_{ij}^{\text{R}} = \sum_{\alpha=1}^M \tau_{ij}^{\alpha}, \quad (24)$$

$$\frac{\lambda^{1,\text{R}}}{\lambda^{\alpha,\text{R}}} \tau_{ij}^{\alpha} + \frac{\mathbf{d}\tau_{ij}^{\alpha}}{\mathbf{d}t} = \kappa_{ij} \mathbf{W}i^{\text{R}} + \kappa_{ij}^{\dagger} \mathbf{W}i^{\text{R}}, \quad (25)$$

where  $\mathbf{d}/\mathbf{d}t$  denotes a co-deformational or Maxwell derivative

$$\frac{\mathbf{d}}{\mathbf{d}t} Q_{ij} = \frac{\mathbf{d}Q_{ij}}{\mathbf{d}t} - \mathbf{W}i^{\text{R}}(\kappa_{il} Q_{lj} + Q_{il} \kappa_{lj}^{\dagger}). \quad (26)$$

$\lambda^{\alpha,R}$  is the time constant for mode  $\alpha$  and  $Wi^R = \lambda^{1,R}\dot{\gamma}$  (or  $\lambda^{1,R}\dot{\epsilon}$ ). The stress has been made dimensionless with  $n_p kT$  and time is made dimensionless with the time constant for the slowest mode in the chain,  $\lambda^{1,R}$ . In the limit of large  $M$ , the ratio of the relaxation time for mode  $\alpha$  to that of the slowest mode scales as  $1/\alpha^2$  [11]. Each mode evolves independently and on a different time scale. Analytic solutions for the stress exist for the inception of shear and extensional flow [10].

The dimensionless birefringence for the Rouse model is

$$\Delta' = \frac{1}{5} \left[ \left\langle \sum_{\alpha=1}^M (\tau_{11}^{\alpha} - \tau_{22}^{\alpha}) \right\rangle^2 + 4 \left\langle \sum_{\alpha=1}^M \tau_{12}^{\alpha} \right\rangle^2 \right]^{1/2}. \quad (27)$$

The Rouse model birefringence has been made dimensionless in the same way as the bead-rod chain and FENE dumbbell, i.e. with  $n_p(\alpha_1 - \alpha_2)(4\pi/3)((n^2 + 2)^2/6n)$  and the dimensionless stress-optic coefficient is  $1/5$ .

## 5. FENE-PM chain

The linear springs in the multimode Rouse chain can be replaced by  $M$  FENE springs but the model can not be solved analytically for a general linear flow [10]. Bird et al. [28] used the Peterlin approximation which replaces the squared length of each spring in the denominator of the FENE spring force with the configurational average squared length and is termed the FENE-P chain. Wedgewood et al. [47] developed a simpler constitutive equation by replacing the squared length of each spring in the denominator of the FENE force law with the average taken over all configurations and springs in a chain. This model is referred to as the FENE-PM chain. Note that for  $M=1$  the FENE-PM model is the same as the FENE-P model. The properties of the FENE-PM model are numerically much simpler to calculate than those of the FENE-P model. Using Brownian dynamics simulations, van den Brule [48] compared FENE, FENE-P and FENE-PM chains with  $M=9$  in shear and uniaxial extensional flow. Both the start-up and steady-state rheology of the chains were reported. He found that the FENE-P and FENE-PM models have very similar rheological behavior which is in close agreement with the FENE model in elongational flow but these models fall to describe FENE shear rheology. Similar conclusions were drawn by Herrchen and Öttinger [44] and Keunings [43] in comparing FENE and FENE-P dumbbells.

After using the FENE-PM averaging, the resulting set of differential equations for the polymer stress can be transformed with the same normal coordinates utilized in the Rouse model to a coupled set of differential equations [47]. The nondimensional constitutive equation for the FENE-PM chain is

$$\tau_{ij}^{\text{FENE-PM}} = \sum_{\alpha=1}^M \tau_{ij}^{\alpha}, \quad (28)$$

$$\frac{\lambda^{1,R}}{\lambda^{\alpha,R}} Z \tau_{ij}^{\alpha} + \frac{d\tau_{ij}^{\alpha}}{dt} - (\tau_{ij}^{\alpha} - 1) \frac{d \ln(Z)}{dt} = \kappa_{ij}^{\alpha} Wi + \kappa_{ij}^{\dagger \alpha} Wi, \quad (29)$$

$$Z = 1 + \frac{3}{b} \left[ 1 - \frac{\tau_{ii}^{\text{FENE-PM}}}{3M} \right]. \quad (30)$$

The stress has been made dimensionless with  $n_p kT$  and time with the time constant of the slowest mode in the chain,  $\lambda^{1,R}$ . The relaxation spectrum for the FENE-PM chain is the same as that for the Rouse chain since they are both transformed into the same normal coordinates. We solved this system of coupled differential equations numerically using a fourth order Runge–Kutta method [49]. Note that in rigorously modeling a chain with a fixed number of Kuhn-steps, the number of modes and the extensibility parameter in the FENE-PM springs should not be varied independently and for large chains are they related by the condition  $3b \times M = N$  [45,47].

The dimensionless birefringence for the FENE-PM model is [11,47]

$$\Delta' = \frac{1}{5} \left[ \left\langle \sum_{\alpha=1}^M (\tau_{11}^{\alpha} - \tau_{22}^{\alpha}) Z \right\rangle^2 + 4 \left\langle \sum_{\alpha=1}^M \tau_{12}^{\alpha} Z \right\rangle^2 \right]^{1/2}. \quad (31)$$

The FENE-PM birefringence has been made dimensionless in the same way as the bead-rod chain, Rouse model and FENE dumbbell, that is, with  $n_p(\alpha_1 - \alpha_2)(4\pi/3)((n^2 + 2)^3/6n)$  and the dimensionless stress-optic coefficient is 1/5.

## 6. Start-up of extensional flow

In this section we will discuss the inception of uniaxial elongational flow. The polymer contribution to the viscosity is defined by the relation:

$$\eta^p = \frac{\tau_{11}^p - \tau_{22}^p}{\text{Pe}}, \quad (32)$$

where the viscosity has been made dimensionless with  $\eta_p \xi a^2$ .

The instant the flow becomes nonzero, the viscous contribution to the viscosity becomes nonzero or there is a ‘stress jump’. Since the chains are initially in their equilibrium configurations, this initial viscosity jump is equal to the low Wi steady-state value which we have previously shown to be  $0.124N - 0.156$  [1]. This value is within 2% of the stress-jump predicted by the multibead-IV model,  $0.126N$  [17]. In Fig. 1 we show the short-time extensional viscosity scaled by  $N - 1$  versus time. The elastic contribution is initially zero and increases with time. Both the elastic and viscous contributions for many  $N$  and Wi can be collapsed onto universal curves by scaling the viscosity with  $N - 1$ . The viscous contributions are relatively constant over these small times and remain at their initial value. The scaling of the elastic part of the viscosity can be understood by considering the evolution of the Rouse extensional viscosity (or shear viscosity since at short times they only differ by a factor of three).

The Rouse model predicts that the stress in each mode will grow like  $a^{\alpha} = (1 - \exp(-t/a^{\alpha}))$  where  $a^{\alpha}$  changes with each mode  $\alpha$  [10]. Thus at short times all the modes will contribute an order  $t$  amount to the stress giving a total stress of order  $Mt$ . This scaling holds very well for the elastic component of the stress in the bead-rod chains if we set the number of modes in the chain equal to the number of rods ( $M = N - 1$ ). The time at which the elastic and viscous contributions are equal is approximately 0.075 (or equivalently  $5.3\lambda_1/N^2$ ). Note that this is a

universal result for all  $N$  and  $Wi$ . For large chains, the time of 0.075 is only a small fraction of the longest relaxation time of the chain (for  $N = 1000$  the longest relaxation time is 14200) and is on the order of the smallest relaxation time in the chain, i.e. the characteristic relaxation time of an individual isolated link (0.0833) [11]. Since the magnitude of the short time viscous contributions are so small and the time scale over which they are larger than the elastic contributions is also very small, they can be considered insignificant. We have confirmed that during the start up of the shear flow the viscosity (scaled by a factor of three) will also follow the same master curves at short times for all  $N$  and  $Wi$ .

In Fig. 2 we show the polymer Trouton ratio (the polymer extensional viscosity divided by the polymer steady-state zero-shear viscosity  $((N^2 - 1)/36$  [10]) versus strain ( $Pe \ t$ ) for  $N = 50$  and various  $Wi$ . Note that the strain is equal to the dimensional time multiplied by the dimensional strain rate. For strains  $< 2$ , the total viscosity at a given strain decreases with increasing  $Wi$  and yet  $> 2$ , the trend reverses. This same trend is observed in the Rouse and FENE model. We have also performed non-Brownian simulations in which we have set the Brownian forces equal to zero and denote these as  $Wi = \infty$ . The viscosity for the non-Brownian simulations,  $Wi = \infty$  and the  $Wi = 35.5$  results are indistinguishable for strains  $> 1$ . In Fig. 3 we have plotted the viscous component along with the total viscosity for several values of  $Wi$ . Note that at  $Wi = 35.5$  the Trouton ratio is still dominated by the elastic contribution. Thus the collapse of the data onto a single curve when plotted as Trouton ratio versus strain does not necessarily mean that the stress is mostly viscous. The transient elastic stress can appear to be viscous in that it is linear in the strain-rate. If one stops the flow, these elastic stresses will decay with a finite rate which we will discuss in a companion publication [67]. This is similar to the steady-state extensional stress for bead-rod chains [1] and FENE dumbbells [10] which at large  $Wi$  scales with  $Wi$  but is dominated by the elastic contributions. In Fig. 4 we have plotted the Trouton ratio versus strain for  $N = 50, 100, 200$  at  $Wi = 10.65$ . As  $N$  increases, the Trouton

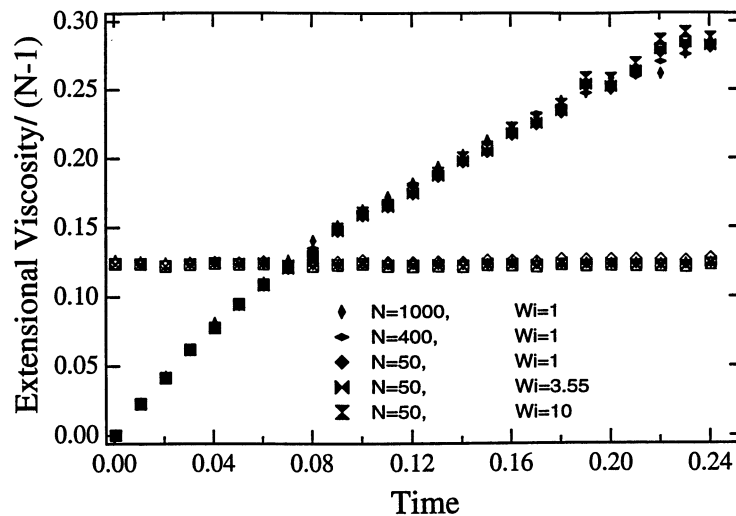


Fig. 1. Short-time extensional viscosity scaled with  $N - 1$  versus time. The empty symbols denote the viscous contribution and the solid symbols the Brownian contribution.

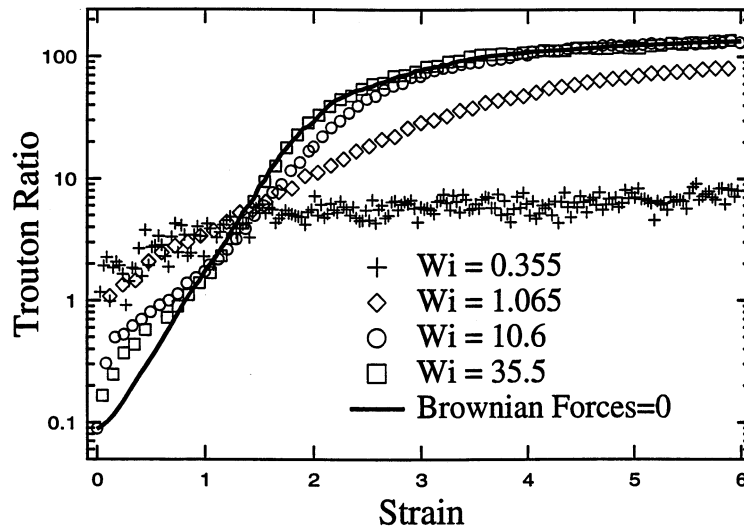


Fig. 2. Trouton ratio versus strain for  $N = 50$  and  $Wi = 0.355, 1.065, 10.65$  and  $35.5$ . The solid line is for a simulation in which the Brownian forces are set to zero and corresponds to  $Wi = \infty$ .

ratio becomes increasingly dominated by the elastic contributions. For  $N = 200$ , the purely viscous contribution to the viscosity is approximately two orders of magnitude smaller than the total viscosity for strains  $> 1$ .

In Fig. 5(a) we have plotted the stress-optic coefficient versus strain for  $N = 50$  and several values of  $Wi$ . The solid lines are calculations based on the radius of gyration which are discussed below. Note that in uniaxial extensional flow there is only one nonzero material function, i.e. the extensional viscosity and hence only one stress-optic coefficient. For small strains the stress-optic

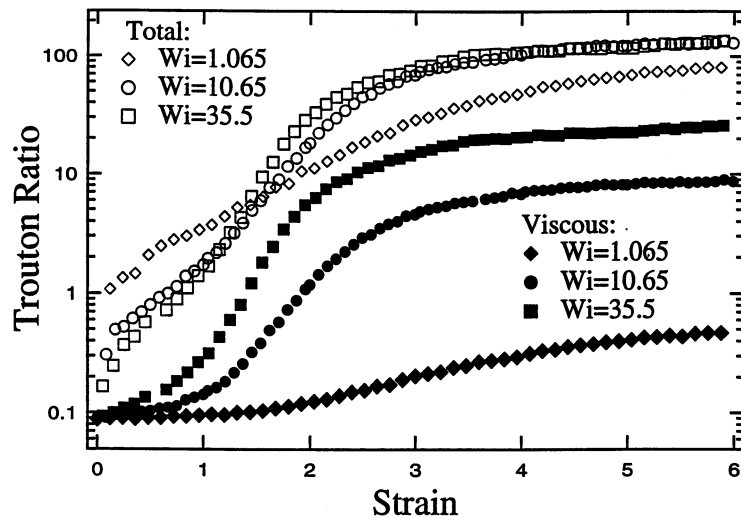


Fig. 3. Trouton ratio and viscous component versus strain for  $N = 50$  and  $Wi = 1.065, 10.65$  and  $35.5$ .

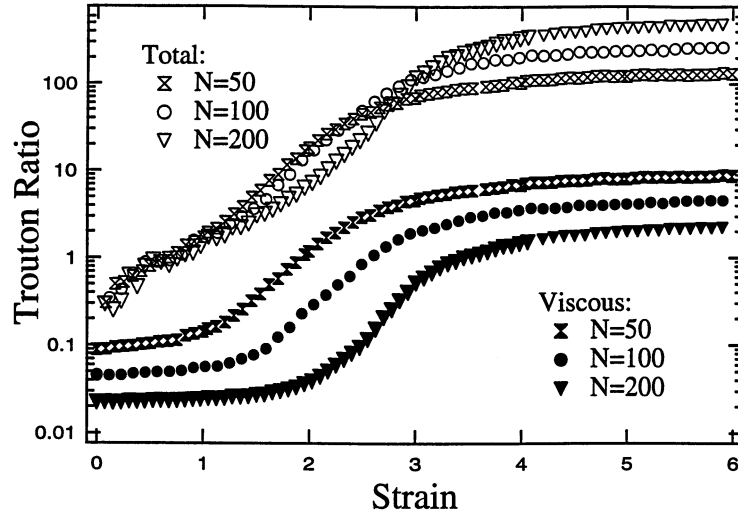


Fig. 4. Trouton ratio and viscous component versus strain for  $N = 50, 100, 200$  and  $Wi = 10.65$ .

coefficient is approximately 0.2 which is in good agreement with the steady-state small  $Wi$  value [1]. For  $Wi \geq 1$  the stress-optic coefficient begins to decrease at strains  $\sim O(1)$ . This is in agreement with the recent experimental data of Spiegelberg and McKinley [33]. As the  $Wi$  increases, the stress-optic coefficient decreases at any given strain. In Fig. 5(b) the stress-optic coefficient is plotted for a fixed value of  $Wi = 10.65$  and  $25 \leq N \leq 200$ . As  $N$  increases, the strain where the stress-optic coefficient begins to decrease also increases. Note that for all  $Wi$  in Fig. 5 the stress is mostly elastic and thus the decrease in the stress-optic coefficient cannot be attributed to a viscous stress. The decrease is due to the large nonlinear elastic stresses caused by stretching of the chain and large length scale correlations in the orientation of the connecting rods. For completely straight chains the elastic stress can be as large as  $N^3/3$  [1,24].

A measure of the overall chain stretch is the radius of gyration:

$$R_g^2 = \frac{1}{N} \sum_{\nu=1}^N R_i^\nu R_i^\nu. \quad (33)$$

In the FENE dumbbell, deviations from a constant stress-optic coefficient occur when the end-to-end distance of the dumbbell is comparable to the maximum dumbbell length. With this in mind, we have constructed a FENE-like stress-optic coefficient:  $0.2[1 - (R_g/R_{g,\infty})^2]$  where  $R_{g,\infty}$  is the radius of gyration for a straight chain. In the FENE model the birefringence is proportional to  $Q_i Q_j$  while the stress is proportional to  $Q_i Q_j / (1 - Q^2/Q_0^2)$ . If the bead-rod chain were to act as a FENE dumbbell, then  $1 - (R_g/R_{g,\infty})^2$  would correspond to the degree of nonlinearity of the stress and the magnitude of the stress-optic coefficient would be  $0.2[1 - (R_g/R_{g,\infty})^2]$ . We have chosen to use the radius of gyration instead of the end-to-end distance because it contains more information about the internal configuration of the chain and also because the radius of gyration can be experimentally measured via light scattering [50]. Using the end-to-end distance did not qualitatively change the results. In Fig. 5 the stress-optic coefficient is compared to  $0.2[1 - (R_g/R_{g,\infty})^2]$ . Although the shape of the radius of gyration curves in Fig. 5 are similar

to those for the stress-optic coefficient, there is no exact match to the transient response of the stress-optic coefficient. The radius of gyration term responds more slowly to the flow than the stress-optic coefficient for all  $N$  and  $Wi$ . If we look at a sample chain as it is unraveled by the flow we see that it initially forms a series of backloops [8,19,23,38]. The non-linear elastic stress is created by the correlated alignment of individual rods in the backloops. Thus the correct length scale for the nonlinear stress is some fraction of the total length of the chain. At longer times the chain becomes substantially unraveled and the degree of nonlinearity is more closely correlated with the radius of gyration of the chain. In a sense the chain is acting like a nonlinear multi-mode model and by describing the nonlinear stresses by the largest length of the polymer, or slowest mode, we fail to capture the short-time dynamics.

The birefringence versus strain is shown in Fig. 6(a) for  $N = 50$  and a range of  $Wi$ . For  $Wi \geq 1$ , the birefringence increases to a significant fraction of the maximum value of  $\Delta' = 49$ . While the viscosity for  $Wi = 35$  and  $Wi = \infty$  were indistinguishable in Fig. 2 beyond a strain of 1, the magnitude of the birefringence is substantially different. For example, at a strain of 2 the ratio of the  $Wi = 35$  to the  $Wi = \infty$  viscosity is 0.99 while the ratio of the birefringence is 0.69.

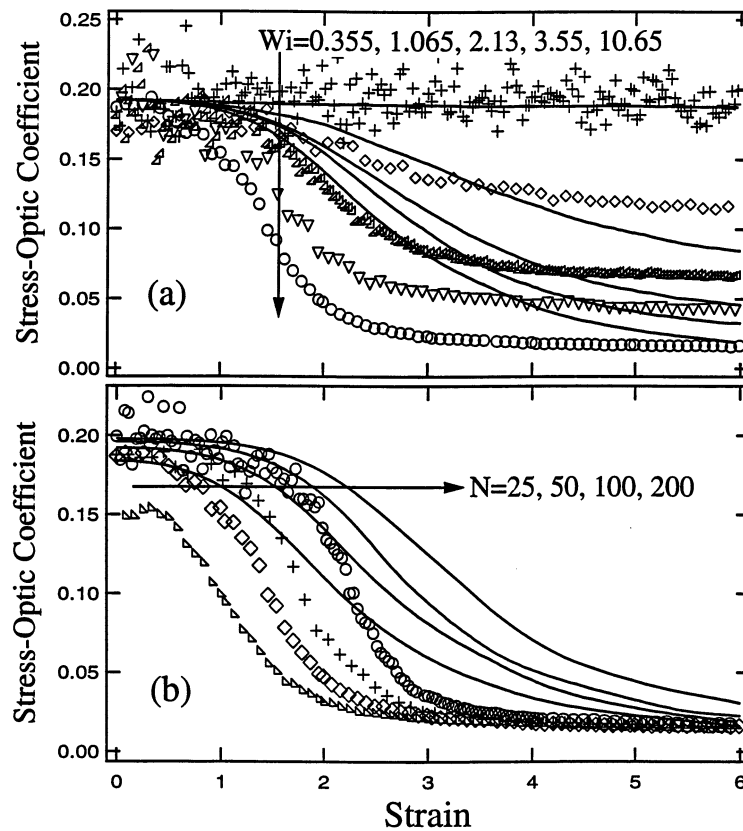


Fig. 5. The stress-optic coefficient versus strain (symbols) and comparison to the FENE-like term  $0.2[1 - (R_g/R_{g,\infty})^2]$  (solid lines). In (a)  $N = 50$  and  $Wi = 0.355, 1.065, 2.13, 3.55$  and  $10.65$ ; and in (b)  $N = 25, 50, 100$  and  $200$  and  $Wi = 10.65$ .

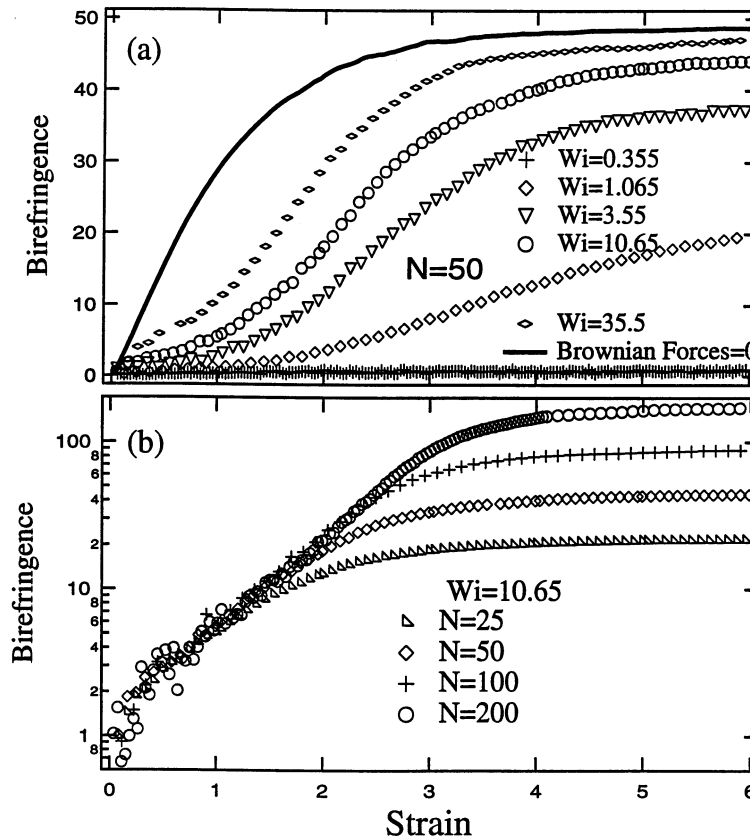


Fig. 6. The birefringence in extensional flow versus strain for (a)  $N = 50$  and  $Wi = 0.355, 1.065, 2.13, 3.55$  and  $10.65$ ; and (b)  $Wi = 10.65$  and  $N = 25, 50, 100$  and  $200$ . In (b) the data is plotted in a semilog manner to show the collapse of the curves at short times which does not occur in (a).

In Fig. 6(b) the birefringence versus strain is shown for  $Wi = 10.65$  and a range of  $N$ . At small strains the curves collapse onto a single curve which increases exponentially in time as would be predicted from the linear Rouse model [10]. Deviations from the exponential behavior occur at larger strains as  $N$  increases due to the finite length of the chain. The point at which the birefringence deviates from exponential growth can be considered as one indication of the nonlinear dynamics of the chain. Another indication of nonlinear dynamics is the decrease of the stress-optic law from the low strain constant value. Comparing the strain at which these occur in Fig. 6(b) and 5(b) we find that the stress-optic coefficient departs from the linear behavior at much smaller strains than the birefringence does. For  $N = 100$ , the stress-optic coefficient begins to decrease at a strain of 1.5 while the birefringence grows exponentially until a strain of 2.5.

### 6.1. Comparison between bead-rod simulation and FENE, Rouse, FENE-PM models

In this section the bead-rod chain extensional viscosity is compared to the FENE, Rouse and FENE-PM models. The polymer viscosity for all the models has been made dimensionless with

$n_p kT \lambda_{\text{model}}$  where  $\lambda_{\text{model}}$  is the longest relaxation time for a given model. Note that the polymer stress (in units  $n_p kT$  for all models) is the dimensionless viscosity multiplied by  $Wi$ .

The start-up of the extensional viscosity for the bead-rod chains with  $N = 50$ , a FENE dumbbell with  $b = 150$  and a five-mode FENE-PM chain with  $b = 30$  are compared in Fig. 7. Note, the corresponding  $b$  for  $N = 50$  is 150. We have chosen to use 5 modes in the FENE-PM model because we are setting  $b = 3N/M$  and we do not want a small value for  $b$ . Ideally, neither  $b$  nor  $M$  should be too small [45,47]. The FENE dumbbell underpredicts the bead-rod extensional viscosity for all strains at  $Wi = 1.065$ , but is in good agreement with the viscosity at  $Wi = 3.55$  and  $Wi = 10.65$  at large strains. The FENE-PM model is in better agreement with the small strain (below about 1.5) viscosity because of the multiple modes. At intermediate strains of 1.5–3 the FENE-PM chain underpredicts the viscosity and at large strains shows a more

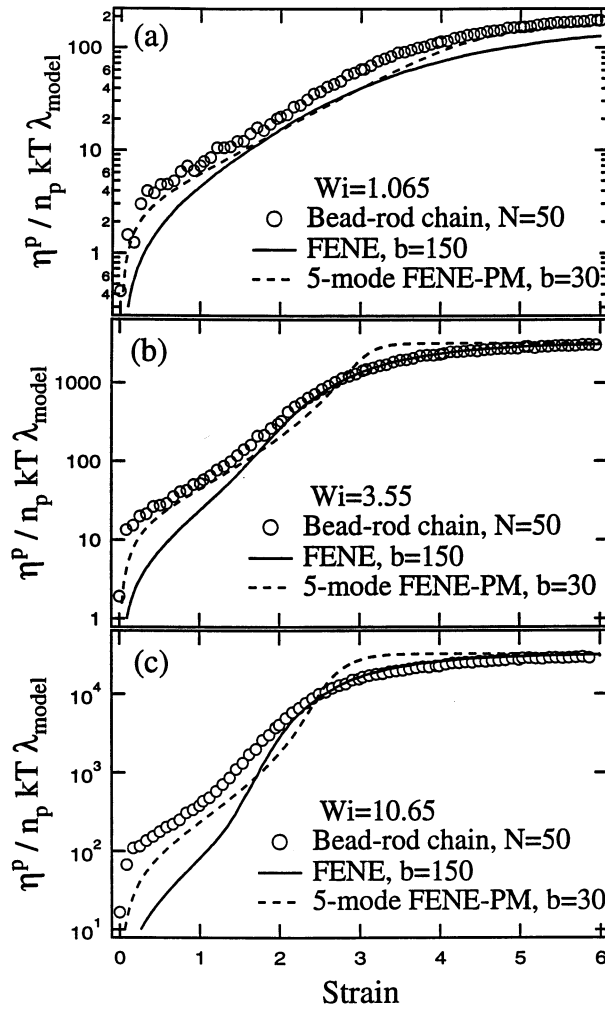


Fig. 7. Comparison (a–c) of polymer viscosity  $\eta^p/n_p kT \lambda_{\text{model}}$  versus strain for the bead-rod chain, FENE dumbbell and FENE-PM model.  $\lambda_{\text{model}}$  is the longest relaxation time for the respective model.

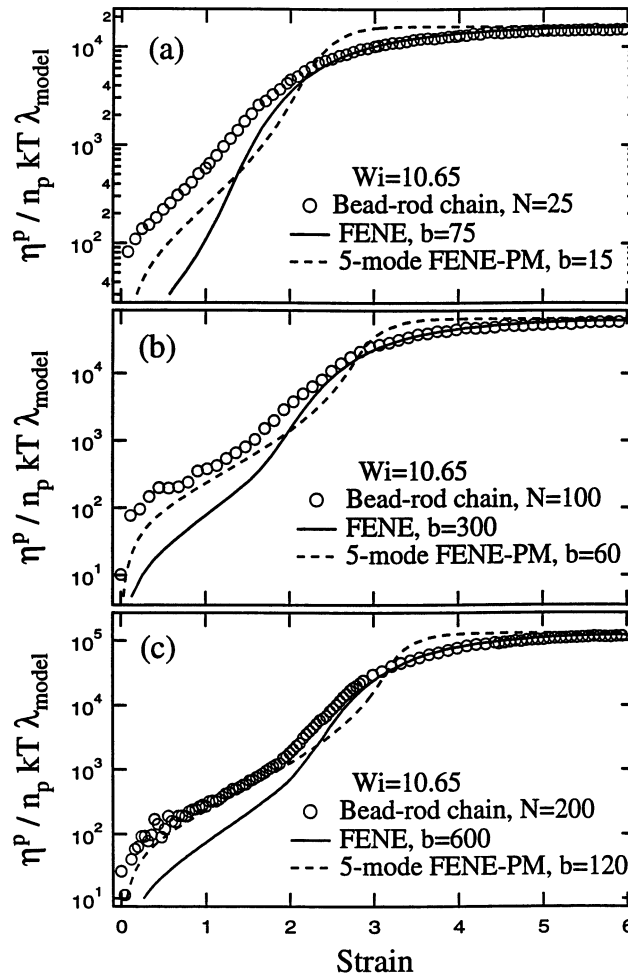


Fig. 8. Comparison of polymer viscosity  $\eta^p/n_p kT \lambda_{\text{model}}$  versus strain for FENE dumbbell, FENE-PM model, and bead-rod chains with  $N =$  (a) 25; (b) 100; and (c) 200.

abrupt approach than the FENE dumbbell or bead-rod chain to the high strain viscosity. Previous studies comparing the FENE dumbbell to a single mode FENE-PM model (FENE-P) have observed similar trends [44].

In Fig. 8 the FENE (with  $b = 3N$ ) and the FENE-PM model (with  $M = 5$  and  $b = 3N/5$ ) are compared to the bead-rod chain at a  $Wi = 10.65$  and varying  $N$  from 25–200. At small strains the FENE-PM model is again in better agreement with the bead-rod chains and the agreement improves with increasing  $N$ . This is to be expected since each mode is representing a larger number of Kuhn steps as  $N$  increases and the original derivation of the entropic spring force is valid in the limit of large  $N$  [25]. At intermediate strains of 2–3 the FENE-PM model underpredicts the viscosity and shows an abrupt approach to the high strain value. The FENE model underestimates the viscosity at small strains and agrees well at large strains. For  $N = 200$  at strains of 2–3 (Fig. 8(c)), both the FENE and the FENE-PM models underpredict the viscosity.

To better understand why the entropic spring models fail to describe the bead-rod extensional viscosity at intermediate strains we show sample chain configurations for  $N = 200$  and  $Wi = 10.65$  in Fig. 9. Initially the chain is in the coiled state and later forms a series of backloops starting at a strain of about 1. At strains of 2–3 the chain has a straight mid-region and the backloops are concentrated at the chain ends. The tensions in the rods in the straight mid-region are much larger than those in the backloops and contribute most to the stress. These configurations are similar to the ‘Yo-Yo’ model proposed by Ryskin [51]. At these strains the chain is not able to fully sample all configurations for a given end-to-end distance which is the fundamental basis for the entropic spring models [25]. At large strains the viscosity approaches the steady state value and the chains adopt almost straight configurations. In these almost straight configurations the number of configurations for a given end-to-end distance decreases greatly and the chains can more easily sample their full configuration space resulting in better agreement with the entropic spring models.

The inability of the FENE dumbbell to capture the short time rheological behavior of the bead-rod chains follows from the fact that it is a single mode model. In Fig. 10 we show the bead-rod chain viscosity and Rouse chains with one, two, five and ten modes. The multi-mode Rouse chain accurately describes the short time rheology but fails to predict a constant long time viscosity (due to the unbound growth of the chain microstructure). Note that by using decreasing  $b$  in the single mode FENE dumbbell the short time viscosity at a given strain increases, but the long time viscosity will decrease. This may serve to explain previous studies [12–15] in which a very small value of  $b$  was needed to match experimental data of Lagrangian unsteady polymeric flows. Ideally then one would want to model the short time (small strain) dynamics with a multi-mode model but at long times the single-mode FENE model is adequate. An important consideration is how many modes are necessary to model the short-time rheology of the bead-rod chains. In Fig. 10 we see that ten modes are enough to quantitatively model the bead-rod chain at short times and even as few as five modes are satisfactory.

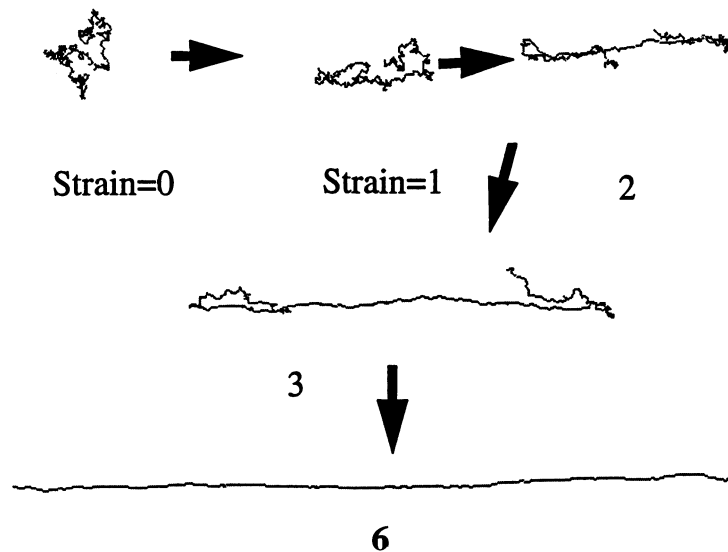


Fig. 9. Sample chain configurations for  $N = 200$  and  $Wi = 10.65$  at strains of 0 to 6.

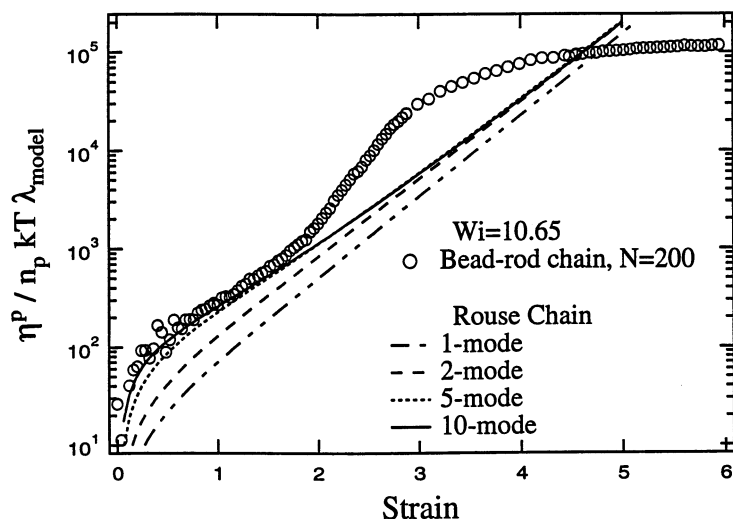


Fig. 10. Comparison of polymer viscosity  $\eta_p/n_p kT \lambda^{1,R}$  versus strain at  $Wi = 10.65$  for a bead-rod chain with  $N = 200$  and the Rouse model with one, two, five and ten modes.

To better understand the extensional rheology of the multimode FENE-PM chain we show the viscosity contribution from each mode for  $M = 5$ ,  $b = 120$  and  $Wi = 10.65$  in Fig. 11. For short times all the modes contribute to the viscosity, just as in the linear Rouse model. Eventually at very high strains the viscosity is dominated by the contribution from the slowest mode and all the other modes decrease to a small magnitude. At intermediate strains of 1–3 the viscosity has significant contributions from modes 1–3 with mode 1 always the largest. Thus

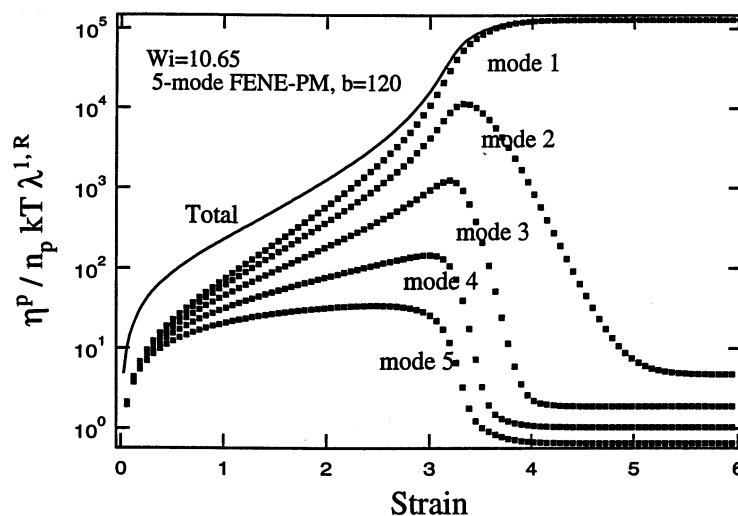


Fig. 11. Polymer viscosity  $\eta_p/n_p kT \lambda^{1,R}$  versus strain for a five-mode FENE-PM chain at  $Wi = 10.65$  and  $b = 120$ . The total stress is the solid line and the contribution from each mode is denoted by the dots.

after deformation at intermediate strain, if the flow were to be switched to some other flow strength ( $Wi$ ) or set to zero the total stress would relax over a spectrum of time scales. This contrasts with the relaxation after deformation at high strains where the stress is dominated by the slowest mode. The extensional rheology of the FENE-PM model is thus similar to a multimode Rouse chain at short times and a single mode FENE dumbbell at longer times; however, the FENE-PM model fails to accurately describe the bead-rod chain rheology at intermediate strains.

## 7. Start-up of shear flow

In this section we will discuss the inception of steady shear flow. The polymer shear viscosity  $\eta^p$  and first normal stress coefficient,  $\Psi_1$ , are defined by the relations

$$\eta^p = \frac{\tau_{12}^p}{Pe}, \quad (34)$$

$$\Psi_1 = \frac{\tau_{11}^p - \tau_{22}^p}{Pe^2}, \quad (35)$$

where  $\Psi_1$  has been made dimensionless with  $n_p \xi a^4 / kT$ . In Fig. 12(a) we show the total shear viscosity scaled by the zero-shear value versus strain and in Fig. 12(b) the viscous contribution for  $N = 50$ . The viscous contribution is approximately an order of magnitude smaller than the total viscosity for all  $Wi$  except at very short times. As in extensional flow, initially the viscous contribution to the viscosity is larger than the elastic for  $t < 0.075$ . The total viscosity shows an overshoot for  $Wi > 3.55$  whereas the viscous contribution shows an overshoot for  $Wi > 10.65$ . The overshoots for  $Wi = 10.65$ ,  $35.5$  and  $106.5$  occur at a strain of  $\approx 7$  for the total viscosity and slightly sooner for the viscous contribution. In Fig. 13 we see that by increasing  $N$  we gradually smooth the overshoots in both the total and viscous contribution to the viscosity. For  $N = 200$  and  $Wi = 35.5$  there is a slight overshoot in the total viscosity and no overshoot in the viscous contribution. In addition, the viscosity becomes increasingly dominated by elastic contributions as  $N$  increases (Fig. 13).

The first normal stress coefficient scaled by the zero-shear value,  $\Psi_{1,0} = 2(N^2 - 1)(10N^3 - 12N^2 + 35N - 12)/(32400N)$  [10], is shown in Fig. 14 for  $N = 50$ . Unlike the viscous contribution to the viscosity, the viscous first normal stress coefficient is initially zero at the inception of flow. For the range of  $Wi$  we have simulated, the viscous contribution to  $\Psi_1$  is always much smaller than the elastic contributions. The total normal stress-coefficient undergoes an overshoot but one that is smaller than observed for the shear viscosity. The viscous contribution to  $\Psi_1$  overshoots at an appreciably smaller strain than the overshoot in the total  $\Psi_1$ . Both the total and viscous  $\Psi_1^p$  overshoots occur at higher strains than for the shear viscosity. In Fig. 15 we see that by increasing  $N$  we smooth the overshoots in both the total and viscous  $\Psi_1$  until for  $N = 200$  neither displays any overshoot. The viscous contribution to  $\Psi_1$  decreases as  $N$  increases and is three orders of magnitude smaller than the total  $\Psi_1$  for  $N = 200$  and  $Wi = 35.5$  (Fig. 15).

In Fig. 16(a) we show the radius of gyration  $R_g/R_{g,0}$  versus strain where  $R_{g,0}$  is the equilibrium radius of gyration,  $R_{g,0} = \sqrt{N}/6$ . For  $Wi > 3.55$  the radius of gyration overshoots the high strain

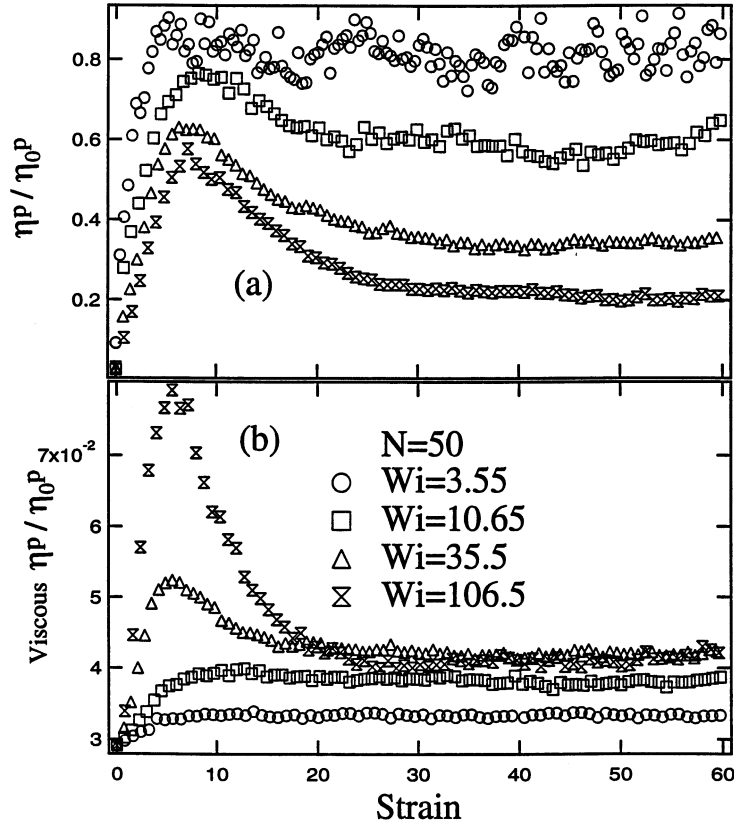


Fig. 12. Total (a) and viscous (b) shear viscosity versus strain for  $N = 50$  and  $Wi = 3.55, 10.65, 35.5$  and  $106.5$ .

value and the magnitude of this overshoot and the strain at which this occurs increases with increasing  $Wi$ . For all  $Wi$ , the radius of gyration at large strain is substantially smaller than the value predicted by the Rouse chain [52],  $R_g^{\text{Rouse}}/R_{g,0}^{\text{Rouse}} = (1 + 0.41Wi^2)^{0.5}$ . The bead-rod chain is less extended than the Rouse chain at a given  $Wi$  due to the nonlinear entropic restoring force as the bead-rod chain is stretched beyond 50% of its contour length. Note though that at  $Wi = 10.65$  the radius of gyration has not reached the maximum possible value of  $R_g/R_{g,0} = 5$  corresponding to a straight chain with  $N = 50$ . In Fig. 16(b) we show the radius of gyration scaled with  $R_{g,0}N^{1/2}$  versus shear strain for  $Wi = 35.5$  and  $N = 50-200$ . We have scaled  $R_g$  with  $R_{g,0}N^{1/2}$  to collapse the large strain values onto a single curve. As  $N$  increases the overshoot in the radius of gyration decreases and for  $N = 200$  there is no overshoot. The overshoots in the material properties  $\eta^P$ ,  $\Psi_1$  and  $R_g^2$  decrease in magnitude as we increase  $N$  at a fixed  $Wi$  because linear shear flow is a weak flow and as we increase  $N$  we expect to recover linear viscoelastic behavior. We note though that this approach to linear behavior can be slow, for example the steady-state shear viscosity approaches the linear value as  $N^{1/3}$  [1]. The Rouse chain predicts that  $R_g/R_{g,0}$  should be independent of  $N$  and equal to 22.8 at  $Wi = 35.5$  which is much more than the value for the  $N = 200$  bead-rod chain of 5.9. For large  $N$ , we expect the bead-rod radius of gyration to approach the Rouse value and we can use the  $N^{0.5}$  scaling to estimate this occurrence

when  $N \approx 3000$  for  $Wi = 35.5$ . This value corresponds to a  $M_w = 3 \times 10^6$  for polystyrene (where we have assumed the Kuhn step to be ten repeat units). Steady-state measurements of  $R_g$  in shear flow using light scattering [53–55] and small angle neutron scattering [56] show smaller deformations than predicted by the Rouse model. For example, Link and Springer found that for dilute polystyrene solutions in a near- $\theta$  solvent ( $M_w = 10^7$ )  $R_g/R_{g,0} = (1 + 0.017Wi^{1.4})^{0.5}$ . Brownian dynamics simulations of Gaussian multibead-spring chains in shear flow have shown that the radius of gyration at a fixed  $Wi$  and  $N$  is decreased by approximately a factor of a half when hydrodynamic interactions are included [57]. Assuming the  $N^{0.5}$  scaling for  $R_g$  holds for large chains, neither the nonlinear restoring forces in the bead-rod model nor hydrodynamic interactions inhibit chain extension enough to be in agreement with the experimental data and we speculate that one needs to account for intra-molecular entanglements in a simulation to capture this.

In Fig. 17(a) we illustrate the stress-optic coefficient versus strain for  $N = 50$  and a range of  $Wi$ . It is remarkable that for a fixed  $Wi$ , the stress optic coefficient based on the 1–2 component of the stress or the difference in the 11–22 components collapse onto a single curve. This collapse occurs for all  $N$  (Fig. 17(b)) and occurs even when the stress-optic coefficient deviates significantly from the constant weak flow value of 0.2. Thus the nonlinear elastic polymer stress

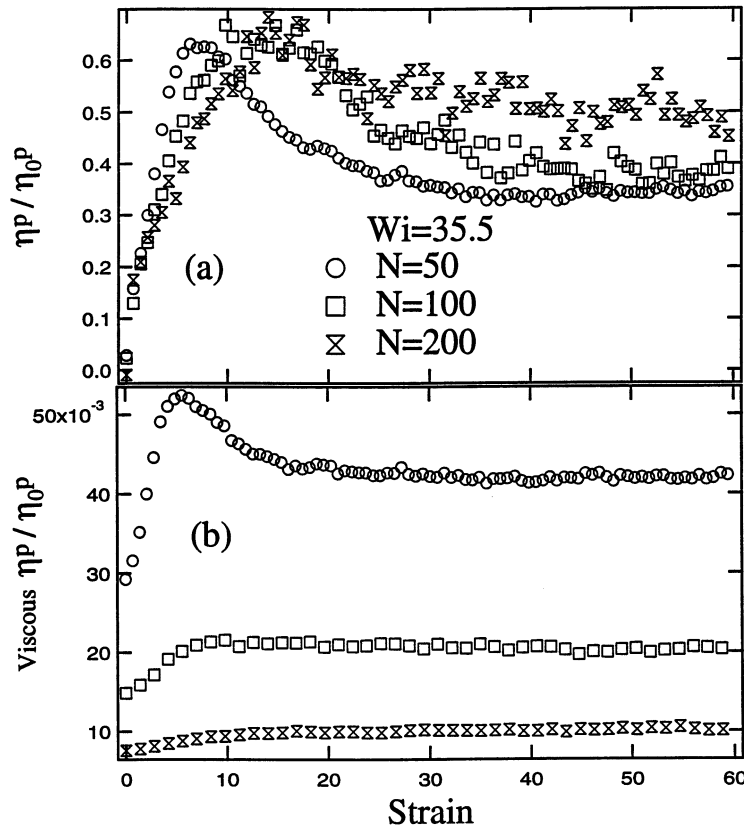


Fig. 13. Total (a) and viscous (b) shear viscosity versus strain for  $N = 50, 100$  and  $200$  and  $Wi = 35.5$ .

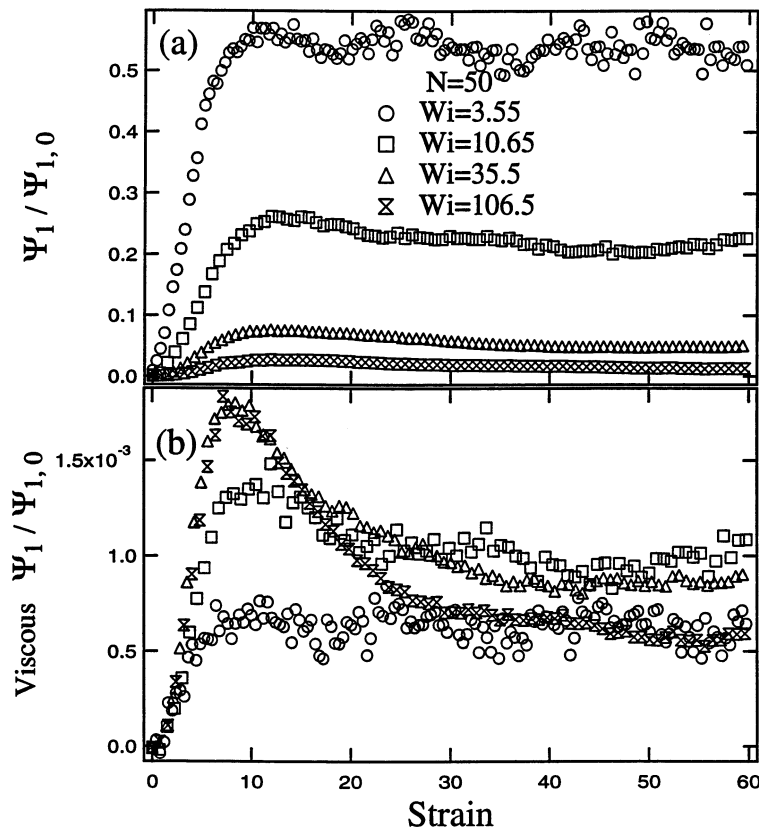


Fig. 14. Total (a) and viscous (b) first normal stress coefficient versus strain for  $N = 50$  and  $Wi = 3.55, 10.65, 35.5$  and  $106.5$ .

tensor is proportional to the polymer index of refraction tensor, but must be multiplied by a scalar quantity which is a function of chain configuration. The modified general stress-optic law for the bead-rod chains is of the form  $\tau_{ij}^p = C(Wi, N)n_{ij}^p$  which is much simpler than the most general form  $\tau_{ij}^p = C_{ijkl}(Wi, N)n_{kl}^p$ .

The solid lines in Fig. 17 denote the FENE-like gyration term  $0.2[1 - (R_g/R_{g,\infty})^2]$ . For  $N = 50$  and  $Wi = 3.55$  in Fig. 17(a), the radius of gyration term is in very good agreement with the stress-optic coefficient but large deviations occur as the  $Wi$  increases. The radius of gyration term underestimates the decrease in the stress-optic coefficient. As  $N$  increases in Fig. 17(b), the long-time value of the radius of gyration term is in slightly better agreement with the stress-optic coefficient but significant differences exist for smaller strains. These results suggest that for moderate  $Wi$  in shear flow, the radius of gyration of a polymer chain can be used in a modified stress-optic law to predict a non-constant stress-optic coefficient which is in quantitative agreement with the actual value in shear flow for  $Wi \leq 3.55$ . For larger  $Wi$ , the FENE-like stress-optic coefficient is larger than the actual value but is an improvement over using the constant low  $Wi$  value. Experimentally one can combine light scattering and birefringence techniques to better estimate nonlinear elastic polymer stresses. Light scattering [53–55] and

small angle neutron scattering [56] have been used in steady flows to measure  $R_g$  though we know of no studies that have measured  $R_g$ , the birefringence and the shear-rate dependent viscosity.

*7.1. Comparison of the bead-rod simulation to the FENE and FENE-PM models*

In Fig. 18  $\eta^p/\eta_0^p$  for  $N = 50$  is compared to a FENE dumbbell with  $b = 150$  and a five-mode FENE-PM model with  $b = 30$ . We have chosen to compare the ratio  $\eta_p/\eta_0^p$  instead of merely  $\eta^p$  because the FENE dumbbell will underestimate the low  $Wi$  shear viscosity (and first normal stress coefficient) because it is a single mode model [10]. For all  $Wi$ , the FENE dumbbell better describes the position and magnitude of the overshoot in the bead-rod viscosity compared to the FENE-PM model. The FENE-PM is in better agreement at short times with the bead-rod chain because it is multimode model, as was the case in extensional flow. In Fig. 19 the shear viscosity at  $Wi = 35.5$  is shown for larger bead-rod chains and compared to the FENE and FENE-PM models. The FENE and FENE-PM models correctly predict that the overshoot in  $\eta^p$  decreases with increasing  $N$ . The agreement between the models does not change as  $N$  increases. Note that in general there is not a large difference in the FENE and the multi-mode FENE-PM viscosity

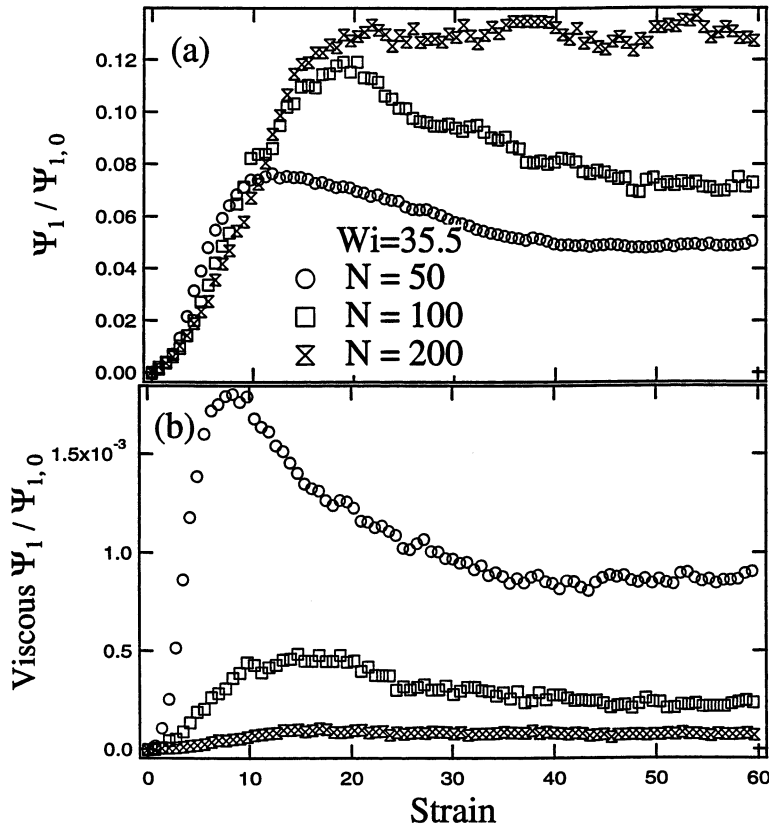


Fig. 15. Total (a) and viscous (b) first normal stress coefficient versus strain for  $N = 50, 100$  and  $200$  and  $Wi = 35.5$ .

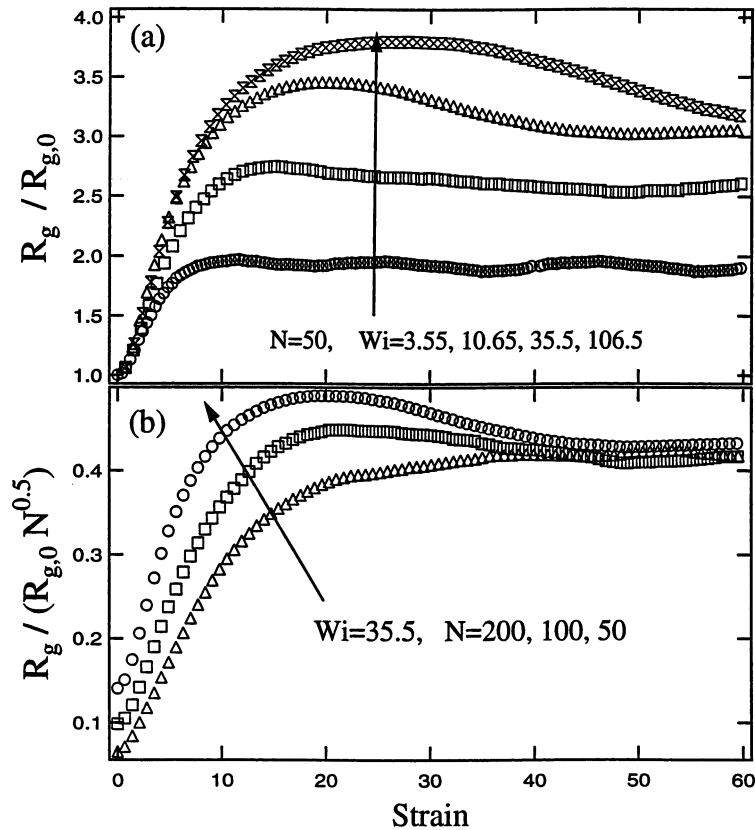


Fig. 16. Radius of gyration divided by the equilibrium value,  $R_{g,0} = (N/6)^{0.5}$ , versus shear strain for  $N = 50$  and  $Wi = 3.55, 10.65, 35.5$  and  $106.5$  (a). Radius gyration divided by  $R_{g,0} N^{0.5}$  versus shear strain for  $Wi = 35.5$  and  $N = 50, 100$  and  $200$  (b).

results; this contrasts with the previous comparisons of a single mode FENE-PM model to FENE dumbbells [44] in which large differences were observed in the magnitude of the overshoot. As we increase the number of modes in the FENE-PM model we expect to recover linear viscoelastic behavior. We have not shown the Rouse model results because at small strain it will coincide with the FENE-PM model and at large strain monotonically approaches a value of 1 [10].

The bead-rod chain first normal stress coefficient is compared to the FENE and FENE-PM models in Fig. 20. As in the viscosity comparisons, we have chosen to compare  $\Psi_1/\Psi_{1,0}$  because the FENE model will underpredict the low shear-rate  $\Psi_1$ . For  $Wi \leq 10.65$  and small strains in Fig. 20, the FENE and FENE-PM chain are in good agreement with the bead-rod chain. At large  $Wi$  and for small strains, the FENE-PM model is still in good agreement with the bead-rod chain while the FENE dumbbell slightly underpredicts  $\Psi_1$ . We can understand the larger discrepancy in comparing the single mode FENE and bead-rod chain viscosity at short times versus comparing the respective values of  $\Psi_1$  by examining the effect of combining multiple linear modes via the Rouse model. In the Rouse model, the characteristic time for the viscosity

and first normal stress coefficient contribution from mode  $\alpha$  is  $\lambda^{\alpha,R}/\lambda^{1,R}$  while weighting of the viscosity is  $\lambda^{\alpha,R}/\lambda^{1,R}$  and the weighting of  $\Psi_1$  is  $(\lambda^{\alpha,R}/\lambda^{1,R})^2$ .  $\Psi_1$  will thus converge faster than  $\eta^p$  when summing many modes. At larger strains, the FENE dumbbell is in much better agreement with the bead-rod chains than the FENE-PM model. As the  $Wi$  was increased, the FENE and FENE-PM models show much larger overshoots in  $\Psi_1$  than the bead-rod chains and the location of the overshoot occurs at larger strains. Herrchen and Öttinger [44] have shown that the averaging in the FENE-PM model for single springs (modes) gives rise to large differences in the transient and steady-state first normal stress coefficient and this is the most likely reason for the poor comparison of the FENE-PM and bead-rod chains. The agreement between the models did not change for increasing chain size of  $N = 100–200$  at  $Wi = 35.5$ , therefore we have not shown these results. Wedgewood and Öttinger [58] have shown that including consistently averaged hydrodynamic interactions, in addition to nonlinear springs, decreases slightly the shear viscosity and first normal stress coefficient overshoots.

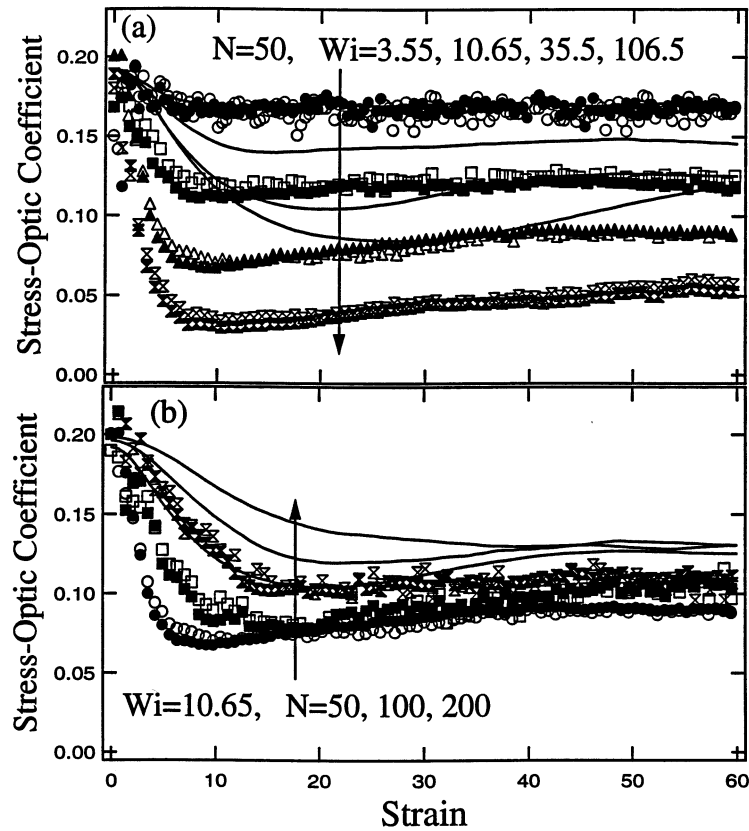


Fig. 17. Stress-optic coefficient versus strain for (a)  $N = 50$  and  $Wi = 3.55, 10.65, 35.5$  and  $106.5$ ; and (b)  $Wi = 10.65$  and  $N = 50, 100$  and  $200$ . The open symbols are the stress-optic coefficient based on the 12 component of the stress and the closed symbols are based on the 11–22 components of the stress. The solid lines are the FENE-like term  $0.2[1 - (R_g/R_{g,\infty})^2]$ .

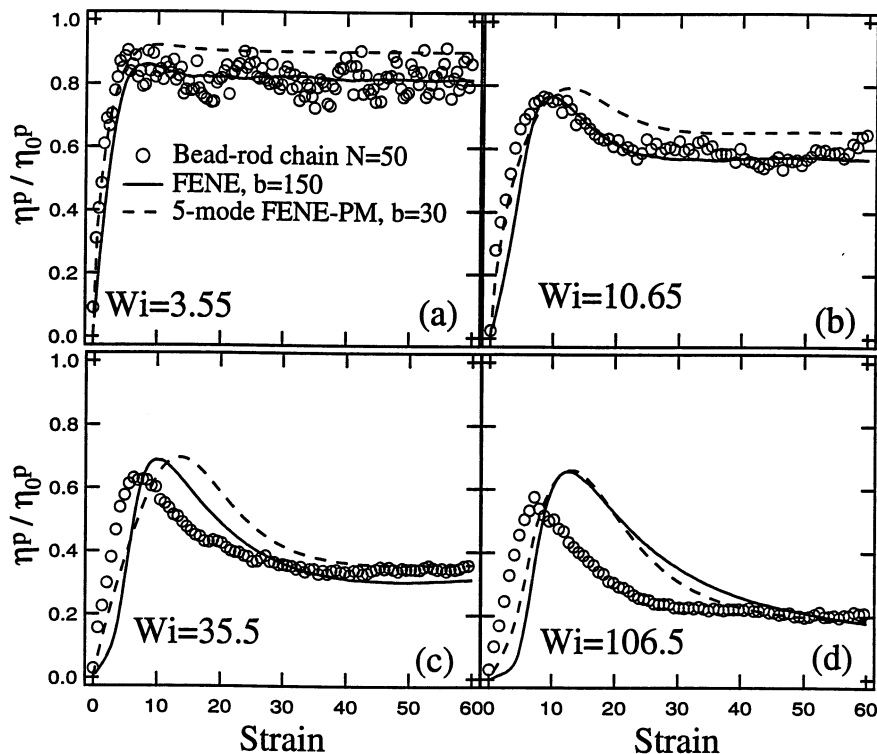


Fig. 18. Comparison of shear viscosity for a bead-rod chain with  $N = 50$ , FENE dumbbell with  $b = 150$  and five-mode FENE-PM model with  $b = 30$  at  $Wi =$  (a) 3.55; (b) 10.65; (c) 35.5; and (d) 106.5.

To better understand the effect of adding multiple modes to the FENE-PM model we show the contribution of each mode to the shear viscosity and first normal stress coefficient Fig. 21(a) and (b) respectively for five modes with  $b = 120$  and  $Wi = 35.5$ . The viscosity has time-dependent contributions from many modes until near the peak of the overshoot after which point all modes  $> 1$  have saturated to a constant value. In contrast, the contributions from modes  $> 1$  to the first normal stress coefficient in Fig. 21(b) are so much smaller than the first mode that they merely appear to contribute a constant offset for strains  $> 10$ . Thus, by adding more modes, the time variation of  $\Psi_1$  is not significantly changed. It follows that one should expect to see similar results for a single mode FENE-PM and thus poor agreement with the FENE dumbbell [44].

## 8. Comparison to experimental data

Our computational resources limit us to simulating bead-rod chains with  $N \leq 200$ , while most experimental results are for polymers with  $N = O(3000)$ . We have shown that the FENE and FENE-PM model can qualitatively describe the bead-rod chain extensional stresses and so we compare these models to experimental data. We recall that quantitative agreement between the FENE-PM and bead-rod chain stress was obtained for small strains whereas the FENE model was in good agreement with the bead-rod chain at large strains.

Recently Spiegelberg and McKinley have measured the extensional viscosity of dilute polystyrene solutions using the filament stretching rheometer [59]. We have compared various elastic polymer models to the data in Fig. 5 in Ref. [59] for a 0.05 wt.% polystyrene solution at  $Wi = 2.84$  [59]. We have subtracted the solvent contribution from the total stress, which for the filament stretching rheometer is approximately [60]

$$\tau_{11}^s - \tau_{22}^s = \left[ 3 + \frac{1}{A_0} e^{-7/3\dot{\epsilon}t} \right] \eta_0^s \dot{\epsilon}, \tag{36}$$

where  $A_0$  is the initial aspect ratio of the sample in the rheometer and  $\eta_0^s$  is the solvent contribution to the zero shear viscosity. Spiegelberg and McKinley [59] let  $A_0 = 0.71$  and  $\eta_0^s = 37.2$  Pa s for their experiments. The polymer contribution to the zero shear viscosity is 10.5 Pa s and the longest relaxation time (from the shear stress relaxation) is  $\lambda_1 = 2.9$  s. We have assumed the polymer has a Zimm spectrum and calculated the contribution from the slowest mode, or equivalently  $n_p kT$ , to be  $\eta^p / \lambda_1 / 2.369 = 1.53$  Pa. The simulation stresses are then made dimensional using  $n_p kT = 1.53$  Pa. The FENE extensibility parameter for the polystyrene is [60]

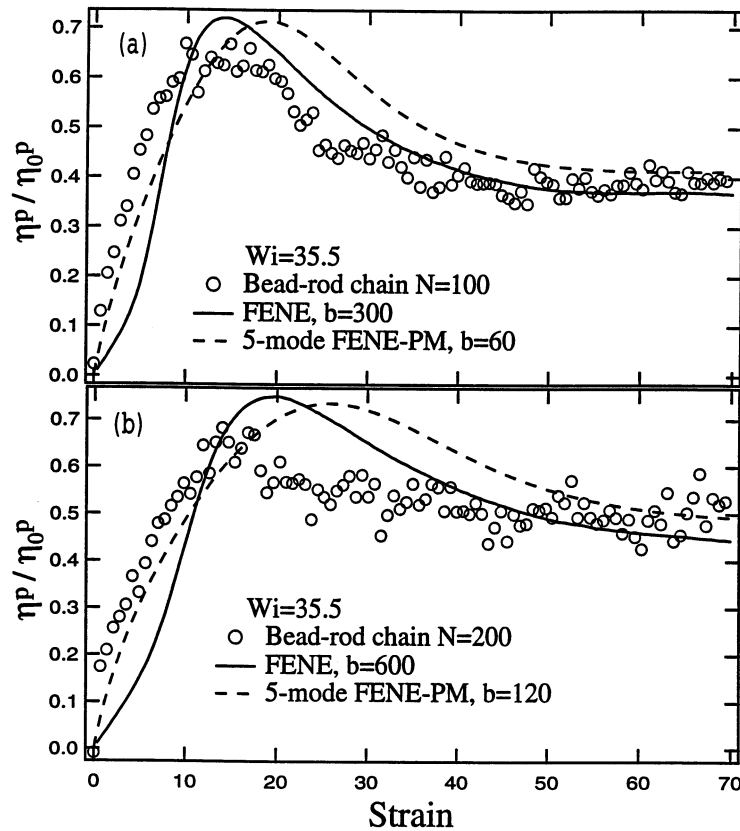


Fig. 19. Shear viscosity versus strain for bead-rod chains, FENE dumbbells and five-mode FENE-PM model at  $Wi = 35.5$ .

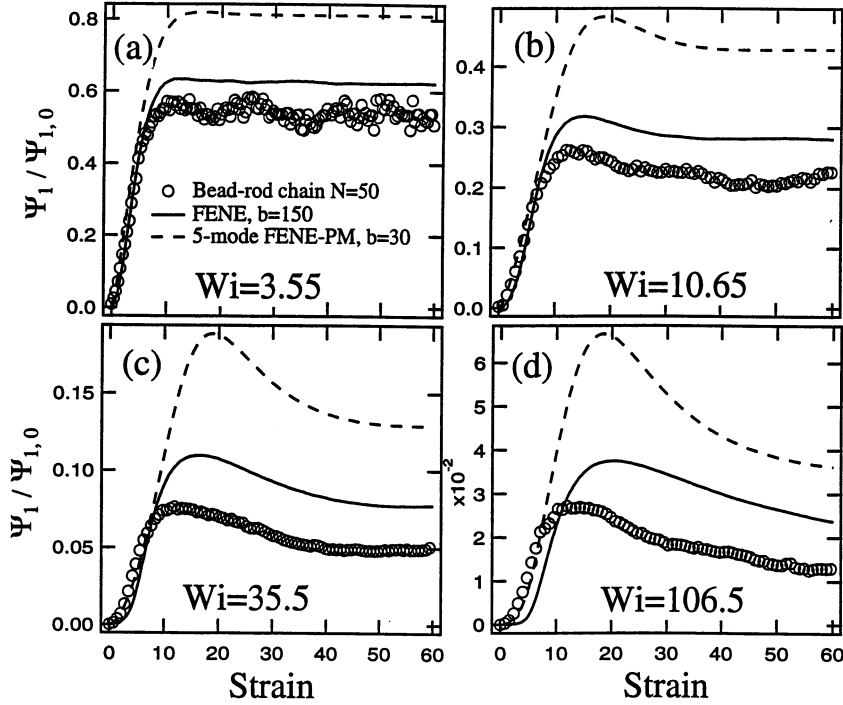


Fig. 20. Comparison of first normal stress coefficient for a bead-rod chain with  $N = 50$ , FENE dumbbell with  $b = 150$  and five-mode FENE-PM model with  $b = 30$  at  $Wi =$  (a) 3.55; (b) 10.65; (c) 35.5; and (d) 106.5.

$$b = \frac{6M_w \sin^2[\tan^{-1}(\sqrt{2})]}{C_\infty M_0}, \quad (37)$$

where  $M_w = 2.25 \times 10^6 \text{ g mol}^{-1}$  is the polystyrene molecular weight,  $M_0 = 104 \text{ g mol}^{-1}$  is the monomer molecular weight,  $C_\infty = 10$  is the characteristic number of monomer units in a Kuhn step and  $2 \tan^{-1}(\sqrt{2}) = \theta = 109.5^\circ$  is the tetrahedral bond angle. For the polystyrene in Ref. [59],  $b = 8665$ .

In Fig. 22(a) we compare the polystyrene stress to a ten-mode FENE-PM model, FENE dumbbell and a ten-mode FENE-PM model where we have modified the relaxation spectrum to have the Zimm form  $\lambda^{i,\text{Zimm}}/\lambda^{1,\text{Zimm}} = i^{-3/2}$  and we denote this model as Zimm-FENE-PM. At small strains, the multimode models are in much better agreement with the experimental data than the single mode FENE, with the Zimm-FENE-PM model giving the best fit. At a strain of 3, the polystyrene stress begins to increase much faster than any of the models and the FENE is in slightly better agreement than the FENE-PM or Zimm-FENE-PM. At large strains all the models predict similar values for stress. Orr and Sridhar [61] have compared the prediction of a multimode FENE-P model (where the modes were independent and obtained from fits to shear data) to extensional stresses for fluid A and also found that it underpredicted the experimental stresses at large strain. They attribute the discrepancy to a viscous stress.

The FENE and FENE-PM models also unpredicted the bead-rod chain extensional viscosity at strains of 3–4, but the discrepancy is not as large as that in Fig. 22(a). One feature which we

have not included in the models is the effects that hydrodynamic interaction will have as the chains are unraveled by the flow. To incorporate this we have performed additional FENE simulations in which we have included a conformation dependent drag coefficient [62–64] which accounts for the additional drag on a uncoiled chain. In our modified FENE simulations we let the drag on a bead increase linearly with the end-to-end distance as

$$\zeta(Q) = \zeta_0 \frac{(Q - \sqrt{3})(\zeta_{\max}/\zeta_0 - 1)}{(\sqrt{b} - \sqrt{3})} + 1, \tag{38}$$

where  $\zeta_0$  is the zero deformation drag and  $\zeta_{\max}$  is the maximum drag when the dumbbell is fully extended. This introduces a new parameter  $\zeta_{\max}/\zeta_0$ . To estimate  $\zeta_{\max}/\zeta_0$ , we have calculated the ratio of the drag on a straight rod to the drag on a Zimm chain [21]

$$\frac{\zeta_{\max}}{\zeta_0} = \frac{6.28L}{\ln(L/d)5.11R}, \tag{39}$$

where  $L$  is the length of the chain,  $d$  is the diameter and  $R$  is the equilibrium root-mean-square end-to-end separation of the chain. The ratio  $L/R$  is equal to  $\sqrt{b/3}$ ,  $d$  is approximately 0.5 nm

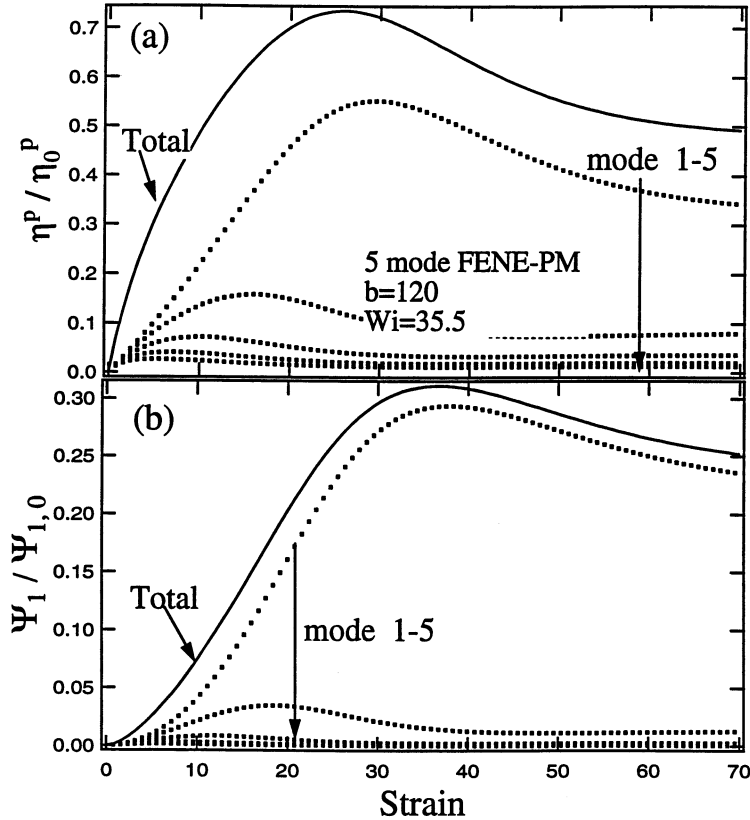


Fig. 21. Shear viscosity (a) and first normal stress coefficient (b) versus strain for a five-mode FENE-PM model with  $b = 120$  and  $Wi = 35.5$ .

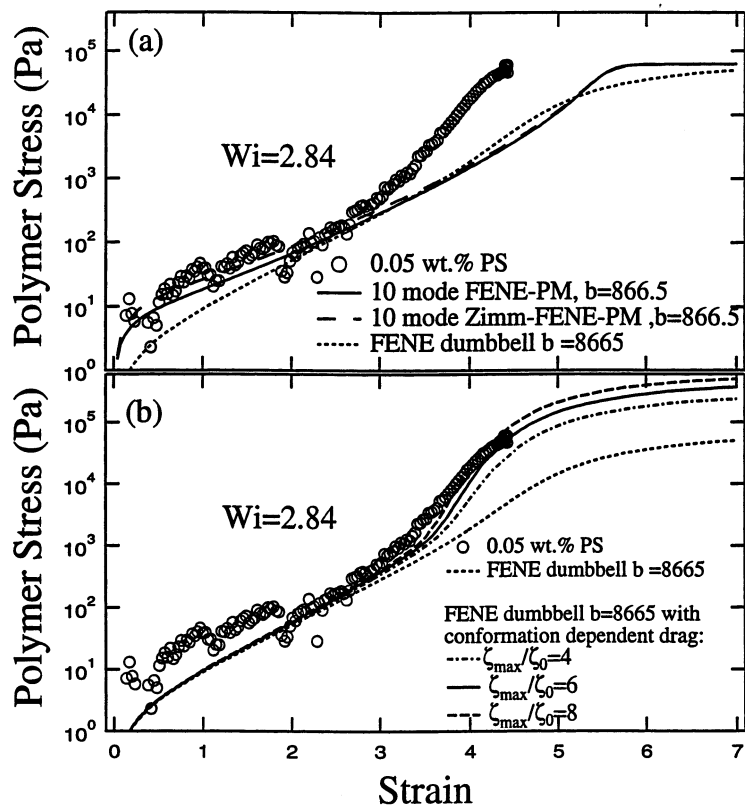


Fig. 22. Comparison of polystyrene extensional stress (from Spiegelberg and McKinley [59]; Fig. 5) at  $Wi = 2.84$  to: (a) ten-mode FENE-PM  $b = 866.5$ , ten-mode Zimm-FENE-PM  $b = 866.5$ , FENE dumbbell  $b = 8665$ ; (b) FENE dumbbells with conformation dependent drag.

and  $L = (b/3) \times 1.54$  nm giving  $(\zeta_{max}/\zeta_0 = 7.3$ . Note that this is much smaller than  $\sqrt{b/3}$  due to the logarithmic term in the straight rod drag [65]. We consider this as an upper bound for  $\zeta_{max}/\zeta_0$  since in the simple single-spring dumbbell model we placed all the drag on two beads at the end of the chain [65].

In Fig. 22(b) the simulation results for the FENE with conformation dependent drag are compared to the polystyrene extensional stress. We show calculations for a FENE without conformation dependent drag and for  $\zeta_{max}/\zeta_0 = 4, 6$  and  $8$ . The conformation dependent FENE models all collapse onto the same curve for small strain because the dumbbell is not significantly extended. At a strain of  $2.5$ , the curves begin to appreciably separate with the stress increasing faster for a larger  $\zeta_{max}/\zeta_0$ . The  $\zeta_{max}/\zeta_0 = 8$  curve is in good agreement with the experimental data and is a marked improvement over the FENE without conformation drag. By increasing the ratio  $\zeta_{max}/\zeta_0$  we decrease the strain at which the FENE model begins to show large nonlinearities in the stress and additionally we change the plateau value of the stress at large strain. In the conformation dependent drag model we are increasing the effective  $Wi$  as the dumbbell extends which gives rise to the stresses increasing at a smaller strain and an increased value in the stress plateau at high strains. The stress plateau increases approximately as  $\zeta_{max}/\zeta_0$ . Fuller and Leal

[64] have compared birefringence measurements of dilute polystyrene solutions in linear flows (measured in the four roll mill device) to a FENE-P model with conformation dependent drag and internal viscosity. They found very good agreement between the model and experimental data. We note though that they used a much larger value for the maximum drag on the dumbbell,  $\zeta_{\max}/\zeta_0 = \sqrt{b/3}$ , than we have used in our comparisons. Experimental studies of DNA molecules in flow [66] suggest that the increase in  $\zeta_{\max}/\zeta_0$  is much smaller than  $\sqrt{b/3}$ . In general though for the FENE models the stress will be more sensitive to changes in the drag ratio  $\zeta_{\max}/\zeta_0$  than the birefringence (or radius of gyration) at large strains where the stress-optic law is no longer valid (at small strains the birefringence and stress are collinear). In addition, at large strains (or at steady-state) the stress will increase linearly with  $\zeta_{\max}/\zeta_0$  whereas the birefringence will be nearly constant as it approaches the maximum value corresponding to full extension and alignment of the dumbbell.

## 9. Conclusions

The rheological and optical properties for bead-rod chains during the inception of uniaxial elongational and shear flow have been presented.

The initial viscous viscosity jump is equal to the low  $Wi$  steady-state value of  $0.124N - 0.156$  and the elastic contribution to the viscosity becomes equal to the viscous when  $t/\lambda_1 = 5.3N^{-2}$  for all  $Wi$  and  $N$ . The elastic stresses quickly become orders of magnitude larger than the viscous stresses for later times. For a fixed  $Wi$ , the stress is dominated by the elastic contribution as  $N$  increases. Additionally, as  $N$  increases the overshoots in the shear viscosity,  $\Psi_1$  and  $R_g$  decrease. We showed that the transient extensional stress can appear to be viscous, in that they can scale linearly in strain-rate, but are truly elastic. This is in direct contrast to the previous studies of Hinch [8] and Rallison [9] which concluded that the transient stresses are mostly viscous for bead-rod chains in extensional flow.

The stress-optic law is valid in elongational flow for  $Wi < 1$ . At larger  $Wi$ , the stress-optic law is constant up to an  $O(1)$  critical strain and the critical strain increases with increasing  $N$ . In shear flow the stress-optic law is no longer valid for  $Wi > 3.55$ . The failure of the stress-optic law in both shear and extensional flow is due to nonlinear elastic stresses. In shear flow, the stress-optic coefficient based the 12 and 11–22 components was the same even when the stress-optic law was not valid suggesting a general stress-optic relation for dilute polymers of the form  $n_{ij} = C(Wi, N)\tau_{ij}^p$  which is much simpler than the most general form  $n_{ij} = C_{ijkl}\tau_{kl}^p$ . The non-constant stress-optic coefficient is in qualitative agreement with the FENE-like term  $0.2[1 - (R_g^y/R_{g,\infty}^y)^2]$  for all  $Wi$  and  $N$  but only quantitatively in agreement for shear flow at  $Wi = 3.55$ .

Having shown that the stress in dilute flexible polymer solutions is mostly elastic, we compared the bead-rod chains to three elastic bead-spring models: FENE, Rouse and FENE-PM. For both shear and extensional flow, a multimode model is needed to resolve the small strain material properties of the bead-rod chains. In extensional flow at large strain, the FENE model with  $b = 3/N$  is in good agreement with the bead-rod chains, but underpredicts the viscosity at small strain. At intermediate strains of 1.5–3 the FENE and FENE-PM models underpredict the bead-rod viscosity because the bead-rod chains cannot sample all configura-

tions for a given end-to-end distance which is an inherent assumption in the entropic spring models. At large strains, the FENE-PM model viscosity is dominated by the contribution from the slowest mode and approaches the single-mode FENE value for the viscosity. A modal decomposition of stress contributions in the FENE-PM model shows that at intermediate strains the elongational viscosity has significant contributions from modes 1–3 but is dominated by mode 1 at long times. Thus, the relaxation of the steady-state stress for the FENE-PM model should be independent of the number of modes for a fixed  $b \times M$ . We will report on the stress relaxation in a future publication [67]. In shear flow the FENE and FENE-PM models gave comparable results for the shear viscosity with the FENE-PM model always being in better agreement with the bead-rod chains at small strain. In contrast, the FENE-PM model predicts a much larger overshoot in  $\Psi_1$  than the FENE or bead-rod models. The addition of multiple modes to the FENE PM model changes significantly the shear viscosity but not the first normal stress coefficient.

The elastic dumbbell models were compared to extensional stress measurements of polystyrene solutions. The FENE-PM model with a Zimm relaxation spectrum was in good agreement with the experimental data for small strain. At large strain the FENE and FENE-PM models underpredict the experimental stress. The FENE simulations with conformation dependent drag, using a modest drag ratio  $\zeta_{\max}/\zeta_0 = 4-8$ , were in best agreement with the experimental data. These results suggest that future Brownian Dynamics studies incorporating hydrodynamic interactions should be performed to better understand their effect on polymer rheology in strong flows. Fetisko and Cummings [68] have performed Brownian Dynamics simulations for small ( $N = 7$ ) multibead FENE chains with excluded volume and hydrodynamic interactions but the effects of hydrodynamic interactions in their extensional flow calculations are secondary to the excluded volume effects (simulating a good solvent).

In a future publication we will report on the relaxation of the elastic bead-rod stresses and compare to the FENE and FENE-PM model [67].

## Acknowledgements

The authors are grateful to Steve Spiegelberg and Gareth McKinley for providing the polystyrene data and for discussions on fitting to the elastic models. This material is based upon work supported by the National Science Foundation under Grant No. DMR-9400354 and support for PSD through a Lieberman Fellowship.

## References

- [1] P.S. Doyle, E.S.G. Shaqfeh, A.P. Gast, Dynamic simulation of freely draining, flexible polymers in linear flows, *J. Fluid Mech.* 334 (1997) 251–291.
- [2] M. Laso, H.C. Öttinger, Calculation of viscoelastic flow using molecular models: the CONNFESSIT approach, *J. Non-Newton. Fluid Mech.* 47 (1993) 1–20.
- [3] K. Feigl, M. Laso, H.C. Öttinger, CONNFESSIT approach for solving a two-dimensional viscoelastic fluid problem, *Macromolecules* 28 (1995) 3261–3274.
- [4] H.C. Öttinger, B.H.A.A. van den Brule, M.A. Hulsen, Brownian configurational fields and variance reduced CONNFESSIT, preprint, 1997.
- [5] M.A. Hulsen, A.P.G. van Heel, B.H.A.A. van den Brule, Simulation of viscoelastic flows using Brownian configuration fields, *J. Non-Newton. Fluid Mech.* (1996), in press.
- [6] E.J. Hinch, Mechanical models of dilute polymer solutions in strong flows, *Phys. Fluids* 20 (1977) 22–30.

- [7] J.M. Rallison, E.J. Hinch, Do we understand the physics in the constitutive equation?, *J. Non-Newton. Fluid Mech.* 29 (1988) 37–55.
- [8] E.J. Hinch, Uncoiling a polymer molecule in a strong extensional flow, *J. Non-Newton. Fluid Mech.* 54 (1994) 209–230.
- [9] J.M. Rallison, Dissipative stresses in dilute polymer solutions, *J. Non-Newton. Fluid Mech.* 68 (1997) 61–83.
- [10] R.B. Bird, C.F. Curtiss, R.C. Armstrong, O. Hassager, *Dynamics of Polymeric Liquids: Kinetic Theory*, Vol. 2, Wiley, New York, 1987.
- [11] R.G. Larson, *Constitutive Equations for Polymer Melts and Solutions*, Butterworth, London, 1988.
- [12] M.D. Chilcott, J.M. Rallison, Creeping flow of dilute polymer solutions past cylinders and spheres, *J. Non-Newton. Fluid Mech.* 29 (1988) 381–432.
- [13] J.V. Satrape, M.J. Crochet, Numerical simulation of the motion of a sphere in a boger fluid, *J. Non-Newton. Fluid Mech.* 54 (1994) 91–111.
- [14] R.A. Keiller, Entry-flow calculations for the Oldroyd-B and FENE equations, *J. Non-Newton. Fluid Mech.* 46 (1993) 143–178.
- [15] J. Azaiez, R. Guenette, A. Ait-Kadi, Numerical simulation of viscoelastic flows through a planar contraction, *J. Non-Newton. Fluid Mech.* 62 (1996) 253–277.
- [16] W. Kuhn, H. Kuhn, *Helv. Chim. Acta* 28 (1945) 1533–1579.
- [17] C.W. Manke, M.C. Williams, Comparison of a new internal viscosity model with other constrained-connector theories of dilute polymer solution rheology, *Rheol. Acta* 32 (1993) 418–421.
- [18] C.W. Manke, M.C. Williams, Transient stress predicted by the internal viscosity model in elongational flow, *Rheol. Acta* 30 (1991) 316–328.
- [19] D. Acierno, G. Titomanlio, G. Marrucci, Dilute solution rheology of flexible macromolecules, *J. Polymer Sci.* 12 (1974) 2177–2187.
- [20] C.W. Manke, M.C. Williams, Transient stress and strain responses predicted by the internal viscosity model in shear flow, *J. Rheol.* 33 (1989) 949–978.
- [21] M. Doi, S.F. Edwards, *The Theory of Polymer Dynamics*, Oxford Science Publications, 1986.
- [22] D.H. King, D.F. James, Analysis of the Rouse model in extensional flow. II Stresses generated in sink flow by flexible macromolecules and by finitely extended macromolecules, *J. Chem. Phys.* 78 (1983) 4749–4754.
- [23] R.G. Larson, The unravelling of a polymer chain in a strong extensional flow, *Rheol. Acta* 29 (1990) 371–384.
- [24] P.S. Grassia, E.J. Hinch, Computer simulations of polymer chain relaxation via Brownian motion, *J. Fluid Mech.* 208 (1996) 255–288.
- [25] L.R.G. Treloar, *The Physics of Rubber Elasticity*, 3rd edn., Clarendon Press, Oxford, 1975.
- [26] W. Kuhn, F. Grun, Relationships between elastic constants and stretching double refraction of highly elastic substances, *Kolloid Z.* 101 (1942) 248.
- [27] H.R. Warner, Kinetic theory and rheology of dilute suspensions of finitely extendible dumb-bells, *Ind. Eng. Chem. Fundam.* 11 (1972) 379–387.
- [28] R.B. Bird, P.J. Dotson, N.L. Johnson, Polymer solution rheology based on a finitely extensible bead-spring chain model, *J. Non-Newton. Fluid Mech.* 7 (1980) 213–235.
- [29] G.G. Fuller, *Optical Rheometry of Complex Fluids*, Oxford University Press, London, 1995.
- [30] W. Philippoff, Studies of flow birefringence of polystyrene solutions, in: *Proc. 4th Int. Cong. Rheology*, Vol. 2, 1965, p. 243.
- [31] W.H. Talbott, J.D. Goddard, Streaming birefringence in extensional flow of polymer solutions, *Rheol. Acta* 18 (1979) 505–517.
- [32] C.A. Cathey, G.G. Fuller, The optical and mechanical response of flexible polymer solutions in extensional flow, *J. Non-Newton. Fluid Mech.* 34 (1990) 63–88.
- [33] S.H. Spiegelberg, G.H. McKinley, Elastic and viscous contributions to stress in extensional rheometry of viscous polymer solutions, in: *XIth Int. Cong. Rheology*, Quebec City, Que, Canada, 1996, pp. 211–212.
- [34] S.F. Smyth, Chen-Hua Liang, M.E. Mackay, G.G. Euller, The stress jump of a semirigid macromolecule after shear: Comparison of the elastic stress to the birefringence, *J. Rheol.* 40 (1995) 659–672.
- [35] C.W. Gardiner, *Handbook of Stochastic Methods*. Springer, Berlin, 1985.
- [36] W.B. Russel, D.A. Saville, W.R. Schowalter, *Colloidal Dispersions*, Cambridge University Press, Cambridge, 1989.
- [37] J.P. Rycksert, G. Ciccotti, J. Berendsen, Numerical integration of the cartesian equations of motion of a system with constraints: Molecular dynamics of *n*-aLkanes, *J. Comput. Phys.* 23 (1977) 327–341.
- [38] T.W. Liu, Flexible polymer chain dynamics and rheological properties in steady flows, *J. Chem. Phys.* 90 (1989) 5826–5842.

- [39] O. Hassager, Kinetic theory and rheology of bead-rod models for macromolecular solutions. (i) Equilibrium and steady flow, *J. Chem. Phys.* 60 (1974) 2111–2124.
- [40] E.J. Hinch, Brownian motion with stiff bonds and rigid constraints, *J. Fluid Mech.* 271 (1994) 219–234.
- [41] J.L.S. Wales, *The Application of Flow Birefringence to Rheological Studies of Polymer Melts*, Delft University Press, Delft, 1976.
- [42] R.M. Kannan, J.A. Kornfield, Stress-optical manifestations of molecular and microstructural dynamics in complex polymer melts, *J. Rheol.* 38 (1994) 1127–1150.
- [43] R. Keunings, On the Peterline approximation for finitely extensible dumbbells, *J. Non-Newton. Fluid Mech.* 68 (1997) 85–100.
- [44] M. Herrchen, H.C. Öttinger, A detailed comparison of various FENE dumbbell models, *J. Non-Newton. Fluid Mech.* 68 (1997) 17–42.
- [45] H.C. Öttinger, *Stochastic Processes In Polymeric Fluids*, Springer, Berlin, 1995.
- [46] P.E. Rouse, A theory for the linear viscoelasticity properties of dilute solutions of coiling polymers, *J. Chem. Phys.* 21 (1953) 1272–1280.
- [47] L.E. Wedgwood, D.N. Ostrov, R.B. Bird, A finitely extensible bead-spring chain model for dilute polymer solutions, *J. Non-Newton. Fluid Mech.* 40 (1991) 199–239.
- [48] B.H.A.A. van den Brule, Brownian dynamics of finitely extensible bead-spring chains, *J. Non-Newton. Fluid Mech.* 47 (1993) 357–378.
- [49] J.H. Fersiger, *Numerical Methods for Engineering Application*, Wiley, New York, 1981.
- [50] P.S. Doyle, E.S.G. Shaqfeh, G.H. McKinley, S.H. Spiegelberg, Relaxation of dilute polymer solutions in extensional flow, *J. Non-Newton. Fluid Mech.* (1997), submitted.
- [51] B. Berne, R. Pecora, *Dynamic Light Scattering: With Applications to Chemistry, Biology and Physics*, Krieger, Malabar, FL, 1990.
- [52] G. Ryskin, Calculation of the effect of polymer additive in a converging flow, *J. Fluid Mech.* 178 (1987) 423–440.
- [53] N. Pistor, K. Binder, Scattering function and the dynamics of phase separation in polymer mixtures under shear flow, *Colloid Polym. Sci.* 266 (1988) 132–140.
- [54] F.R. Cottrell, E.W. Merrill, K.A. Smith, Conformation of polyisobutylene in dilute solution subject to a hydrodynamic shear field, *J. Polym. Sci. A-2* (7) (1969) 1415–1434.
- [55] A. Link, J. Springer, Light scattering from dilute polymer solutions in shear flow, *Macromolecules* 26 (1993) 464–471.
- [56] M. Zisenis, J. Springer, Rheo-optical detection of shear-induced orientation of high molar mass polystyrene in dilute solution, *Polymer* 35 (1994) 3156–3163.
- [57] P. Lindner, R.C. Oberthür, Shear-induced deformation of polystyrene coils in dilute solution from small angle neutron scattering 2. Variation of shear gradient, molecular mass and solvent viscosity, *Colloid Polym. Sci.* 266 (1988) 886–897.
- [58] J.J.L. Cascales, J.G. de la Torre, Hydrodynamic interaction effects on the conformation of flexible chains in simple shear flow, *Macromolecules* 23 (1990) 809–813.
- [59] L.E. Wedgwood, H.C. Öttinger, A model of dilute polymer solutions with hydrodynamic interaction and finite extensibility II. Shear flows, *J. Non-Newton. Fluid Mech.* 27 (1988) 245–264.
- [60] S.H. Spiegelberg, G.H. McKinley, Stress relaxation and elastic decohesion of viscoelastic polymer solutions in extensional flow, *J. Non-Newton. Fluid Mech.* 67 (1996) 49–76.
- [61] S.H. Spiegelberg, D.C. Ables, G.H. McKinley, The role of end-effects on measurements of extensional viscosity in filament stretching rheometers, *J. Non-Newton. Fluid Mech.* 64 (1996) 229–267.
- [62] N.V. Orr, T. Sridhar, Stress relaxation in uniaxial extension, *J. Non-Newton. Fluid Mech.* 67 (1996) 77–103.
- [63] P.G. de Gennes, Coil-stretch transition in dilute flexible polymers under ultrahigh velocity gradients, *J. Chem. Phys.* 60 (1974) 5030–5042.
- [64] E.J. Hinch, *Proc. Symp. Polymer Lubrication*, Brest, France, 1974.
- [65] G.G. Fuller, L.G. Leal, Flow birefringence of dilute polymer solutions in two dimensional flows, *Rheol. Acta* 19 (1980) 580–600.
- [66] R.G. Larson, *The structure and rheology of complex fluids*, 1997, in press.
- [67] R.G. Larson, T.T. Perkins, D.E. Smith, S. Chu, Hydrodynamics of a DNA molecule in a flow field, *Phys. Rev. E* 55 (1997) 1794–1797.
- [68] S.W. Fettsko, P.T. Cummings, Brownian dynamics simulation of bead-spring chains models for dilute polymer solutions in elongational flow, *J. Rheol.* 39 (1995) 285–299.